

A Multi-Level Deep Framework for Deep Solvers of Partial Differential Equations^{*}

Yu Yang^a, Qiaolin He^{a,*}

^a*School of Mathematics, Sichuan University, 610065, Chengdu, China.*

ARTICLE INFO

Keywords:

deep learning
neural network
partial differential equation
multi-level sampling
multi-level training

ABSTRACT

In this paper, inspired by the multigrid method, we propose a multi-level deep framework for deep solvers. Overall, it divides the entire training process into different levels of training. At each level of training, an adaptive sampling method proposed in this paper is first employed to obtain new training points, so that these points become increasingly concentrated in computational regions corresponding to high-frequency components. Then, the generalization ability of deep neural networks are utilized to update the PDEs for the next level of training based on the results from all previous levels. Rigorous mathematical proofs and detailed numerical experiments are employed to demonstrate the effectiveness of the proposed method.

1. Introduction

In recent years, propelled by the wave of artificial intelligence, deep learning has been widely adopted for numerically solving partial differential equations (PDEs). Leveraging the formidable approximation power of deep neural networks, researchers have developed a host of outstanding solvers. From the perspective of function learning, Physics-Informed Neural Networks (PINNs) [13] and Deep Galerkin Method [14] are well known for their use of the strong form of PDEs, whereas Deep Ritz method [22] and Weak Adversarial Network [28] achieve excellent results based on the weak form. From the operator-learning viewpoint, the Fourier Neural Operator (FNO,[10]), and deep operator networks (DeepONet,[12]) serve as representative deep operator-learning models.

Because a deep neural network is a highly nonlinear and over-parameterized complex system, its internal regularities and operating mechanisms constitute a challenging and worthwhile research topic when it is employed to solve PDEs. Xu et al. [25, 26] proposed the frequency principle: when deep networks solve PDEs they typically learn the low-frequency components of the target function first, while high-frequency components are acquired much more slowly. Going further, Tancik et al. [15] analyzed the output of deep networks with the neural tangent kernel (NTK) and showed that the convergence speed of a network is governed by the eigenvalues of the NTK matrix—larger eigenvalues lead to faster convergence. Because low-frequency modes of the target function usually correspond to larger eigenvalues of this matrix, whereas high-frequency modes correspond to smaller ones, Tancik et al. arrive at a conclusion similar to Xu's frequency principle: deep networks preferentially fit the low-frequency content of the target. This behavior, however, is precisely the opposite of what is observed with traditional numerical methods.

Classical numerical methods, such as finite difference, finite volume, and finite element schemes, cast the PDE problem into the solution of a system of linear algebraic equations by means of mesh discretization. The resulting linear systems are then solved iteratively, typically via Gauss–Seidel, Jacobi, or successive over-relaxation (SOR) iterations. These iterative methods are highly effective at rapidly eliminating the high-frequency components of the error, i.e., components that oscillate violently on the grid, but are far less efficient at eliminating the low-frequency components, a behavior that is precisely the opposite of what is observed with deep neural networks. To overcome this limitation, researchers developed the multigrid method. The multigrid method is an efficient numerical algorithm for solving partial differential equations whose core idea is to treat the error on a hierarchy of grids ranging from fine to coarse. High-frequency errors are first damped on the fine grid; the remaining low-frequency residuals are then transferred to a coarser grid, where they reappear as higher-frequency components that are easily reduced. Finally,

^{*} This research is partially sponsored by the National key R & D Program of China (No.2022YFE03040002) and the National Natural Science Foundation of China (No.11971020, No.12371434).

^{*}Corresponding author

✉ yangyu1@stu.scu.edu.cn (Y. Yang); qlhejenny@scu.edu.cn (Q. He)

ORCID(s): 0009-0005-1428-6745 (Y. Yang)

the coarse-grid correction is interpolated back to the fine grid, thereby allowing errors across all frequency bands to be eliminated rapidly. Indeed, combining multigrid methods with neural networks has already been proposed by researchers. A hybrid solution framework is introduced in [5], composed of traditional iterative solvers and PINNs. During the solution process, the iterative scheme eliminates local high-frequency errors, while PINNs correct the low-frequency components. In [7], He et al., inspired by the solution and data spaces of PDE systems, introduce analogous feature and data spaces within a Convolutional Neural Network (CNNs). By regarding an image as a function on a grid and images of different resolutions as functions on grids of varying sizes, they integrate CNNs with multigrid structures and propose MgNet for image-classification tasks. In [3], Chen et al. extend MgNet to develop PDE-MgNet for solving PDEs, further incorporating meta-learning techniques to handle parameterized PDEs.

Inspired by the multigrid methods, we hope to explicitly attenuate the high-frequency components that deep neural networks struggle to learn when solving PDEs. Note that an actual computational grid is not required during training of a deep solver; what is indispensable are the learning samples, i.e., the collocation points. Adaptive sampling techniques that cluster these points in regions dominated by high frequencies have already produced several promising results. In the study [23] introduces a residual-guided adaptive distribution (RAD) technique which builds a probability density from residual magnitudes and then draws new samples according to this density. The contribution in [6] defines a failure probability that serves as an a-posteriori error indicator for placing fresh training data. A different adaptive sampling method for partial differential equations is developed in [17]; it quantifies the variance of the residual loss and exploits the KRNet architecture proposed in [16]. Departing from residual-oriented strategies, [27] presents MMPDE-Net, which borrows the moving-mesh idea: it constructs a monitor function from the current solution and redistributes training points accordingly.

In this paper, we propose a multi-level training framework for deep solvers. Overall, it divides the entire training process into different levels of training. At each level of training, an adaptive sampling method proposed in this paper is first employed to obtain new training points, so that these points become increasingly concentrated in computational regions corresponding to high-frequency components. Then, the generalization ability of deep neural networks are utilized to update the PDEs for the next level of training based on the results from all previous levels. The multi-level training process repeats until a stopping criterion is met or the maximum number of iterations is reached. Indeed, researchers have also investigated methods that split a complete training process into multiple training stages. Different from the focus of our approach, in [24], Xu gradually adjusts the size of the neural network across successive training runs to obtain good results; in [21], Wang et al. vary critical parameters such as the magnitude prefactor and scale factor during multiple training stages to achieve superior performance.

In summary, our contributions in this work are as follows:

- We develop a multi-level sampling method that is driven by the residual of the loss function and the gradient of the objective function; as the level increases, the sampling points become increasingly concentrated in regions corresponding to high-frequency components.
- A multi-level training framework is proposed, where the PDEs at the current level are modified according to the results from all previous levels, and advanced optimization methods are utilized to achieve improved accuracy.
- Rigorous mathematical proofs and detailed numerical experiments are employed to demonstrate the effectiveness of the proposed method.

The remainder of the paper is organized as follows. Section 2 provides a general description of partial differential equations and offers a brief introduction to PINNs. Section 3 presents the proposed multi-level deep framework, covering sampling, training, and optimization, and provides a theoretical error analysis. Section 4 reports numerical experiments that validate the effectiveness of our approach. Concluding remarks are given in Section 5.

2. Preliminary work

2.1. Problem formulation

Consider the following general form of a system of partial differential equations

$$\begin{cases} \mathcal{A}[\mathbf{u}(\mathbf{x})] = f(\mathbf{x}), & \mathbf{x} \in \Omega, \\ \mathcal{B}[\mathbf{u}(\mathbf{x})] = g(\mathbf{x}), & \mathbf{x} \in \partial\Omega. \end{cases} \quad (1)$$

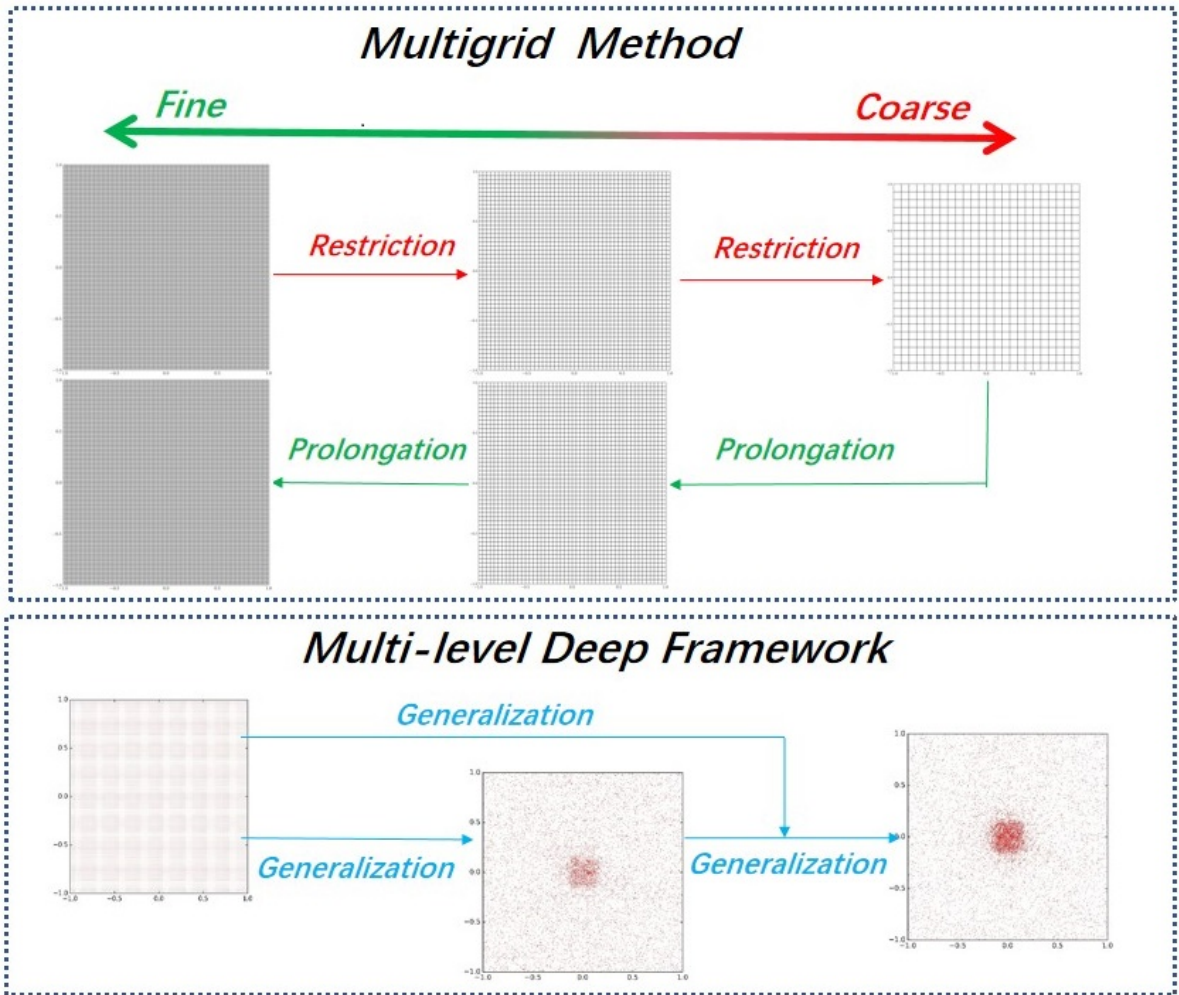


Figure 1: This figure illustrates a comparison between a two-level multigrid method and a multi-level framework. In the multigrid method, computation is first performed on the fine grid, after which the residual is restricted to the coarse grid. An error equation is then solved on the coarse grid to approximate the low-frequency error components that are difficult to eliminate on the fine grid. Finally, the correction obtained on the coarse grid is interpolated back to the fine grid to update the solution there. In the multi-level framework, training is first conducted on uniformly distributed sample points. The generalization capability of the trained neural network and a multi-level sampling strategy are then leveraged to update the set of sample points. A new equation is subsequently solved on these new sample points. Ultimately, the predicted solutions from the different neural networks are summed to yield the final predicted solution for the original equation (for a detailed introduction of our method, please refer to Section 3.1).

where $\mathbf{u}(\mathbf{x})$ is the unique solution of this system.

The interior of the entire computational domain $\Omega \subset \mathbb{R}^d$ is a bounded, open, and connected region, and it has a polygonal boundary $\partial\Omega$. The system is governed by the operator \mathcal{A} and a source term $f(\mathbf{x})$ within the domain Ω , subject to boundary conditions on $\partial\Omega$ prescribed by the operator \mathcal{B} and the function $g(\mathbf{x})$.

2.2. Introduction to PINNs

Unlike traditional neural networks that rely heavily on large datasets, Physics-Informed Neural Networks (PINNs) incorporates physical principles as constraints, enabling the model to maintain scientific consistency even with limited or scarce observed data. The core idea is to embed equation residuals, boundary and initial conditions as part of the loss function, guiding the network to learn solutions that adhere to physical principles.

Let θ denote the parameters of PINNs, let $\mathbf{x} \subset \Omega \cup \partial\Omega$ represent the input to PINNs, and let $\mathbf{u}(\mathbf{x}; \theta)$ denote the output of PINNs, i.e., the predicted solution to the equation 1. Suppose that $r(\mathbf{x}; \theta) = \mathcal{A}[\mathbf{u}(\mathbf{x}; \theta)] - f(\mathbf{x}) \in \mathbb{L}_2(\Omega)$ and $b(\mathbf{x}; \theta) = \mathcal{B}[\mathbf{u}(\mathbf{x}; \theta)] - g(\mathbf{x}) \in \mathbb{L}_2(\partial\Omega)$, the loss function of a general PINN can be expressed as

$$\begin{aligned} \mathcal{L}(\mathbf{x}; \theta) &= \tilde{\alpha}_1 \|\mathcal{A}[\mathbf{u}(\mathbf{x}; \theta)] - f(\mathbf{x})\|_{2,\Omega}^2 + \tilde{\alpha}_2 \|\mathcal{B}[\mathbf{u}(\mathbf{x}; \theta)] - g(\mathbf{x})\|_{2,\partial\Omega}^2 \\ &= \tilde{\alpha}_1 \int_{\Omega} |\mathcal{A}[\mathbf{u}(\mathbf{x}; \theta)] - f(\mathbf{x})|^2 d\mathbf{x} + \tilde{\alpha}_2 \int_{\partial\Omega} |\mathcal{B}[\mathbf{u}(\mathbf{x}; \theta)] - g(\mathbf{x})|^2 d\mathbf{x} \\ &= \tilde{\alpha}_1 \int_{\Omega} |r(\mathbf{x}; \theta)|^2 d\mathbf{x} + \tilde{\alpha}_2 \int_{\partial\Omega} |b(\mathbf{x}; \theta)|^2 d\mathbf{x} \end{aligned} \quad (2)$$

where $\tilde{\alpha}_1$ is the weight of the residual loss and $\tilde{\alpha}_2$ is the weight of the boundary loss.

After sampling training points $\{\mathbf{x}_i\}_{i=1}^{N_r} \subset \Omega$ and boundary training points $\{\mathbf{x}_i\}_{i=1}^{N_b} \subset \partial\Omega$, the empirical loss with a total of $N = N_r + N_b$ training points can be written as

$$\begin{aligned} \mathcal{L}_N(\mathbf{x}; \theta) &= \frac{\tilde{\alpha}_1 V(\Omega)}{N_r} \sum_{i=1}^{N_r} |r(\mathbf{x}_i; \theta)|^2 + \frac{\tilde{\alpha}_2 V(\Omega)}{N_b} \sum_{i=1}^{N_b} |b(\mathbf{x}_i; \theta)|^2 \\ &\triangleq \alpha_1 \sum_{i=1}^{N_r} |r(\mathbf{x}_i; \theta)|^2 + \alpha_2 \sum_{i=1}^{N_b} |b(\mathbf{x}_i; \theta)|^2 \\ &\triangleq \alpha_1 \mathcal{L}_{r,N_r}(\mathbf{x}_i; \theta) + \alpha_2 \mathcal{L}_{b,N_b}(\mathbf{x}_i; \theta). \end{aligned} \quad (3)$$

where $V(\Omega)$ is the volume of Ω . Without loss of generality, we use α_1 to denote the weight of the discrete residual loss function $\mathcal{L}_{r,N_r}(\mathbf{x}_i; \theta)$, and α_2 to denote the weight of the discrete boundary loss function $\mathcal{L}_{b,N_b}(\mathbf{x}_i; \theta)$. Ultimately, the optimization method is employed to minimize the empirical loss $\mathcal{L}_N(\mathbf{x}; \theta)$, steering PINNs toward learning the latent solution of the Eq (1).

3. Main results

3.1. Methods

3.1.1. Multi-level Sampling

In this section, we will elaborate on the sampling algorithm within our Multi-Level depp framework, which named as Multi-Level sampling. The vision of this sampling method is that sampling points can be concentrated in areas with large loss residuals and drastic changes in the predicted solution, and become increasingly concentrated as the level increases. This indicates that the Multi-Level sampling method will be used multiple times in our framework. Below, we will start with the introduction of this algorithm from the first-level.

Let $\mathcal{X}_{N_r}^1 = \{\mathbf{x}_i\}_{i=1}^{N_r} \subset \Omega$ be a set of points obtained through uniform sampling and let the output of the neural network after the first-level training be $u(\mathbf{x}; \theta^1)$. Then, based on the first-level predicted solution $u(\mathbf{x}; \theta^1)$, the first-level residual $r(\mathbf{x}; \theta^1)$ can be obtained.

$$\mathcal{R}(\mathbf{x}; \theta^1) = |\mathcal{A}[u(\mathbf{x}; \theta^1)] - f(\mathbf{x})|. \quad (4)$$

Then, using automatic differentiation, the partial differential terms $\nabla u(\mathbf{x}; \theta^1)$ corresponding to the predicted solution $u(\mathbf{x}; \theta^1)$ can also be obtained, and the following function can be constructed.

$$\mathcal{H}(\mathbf{x}; \theta^1) = \gamma |\nabla u(\mathbf{x}; \theta^1)|, \quad (5)$$

where γ is a given constant. Following the guidance of Eq (4), sampling points can be concentrated in regions with larger residuals and sharp gradients. Similarly, Eq (5) enables the concentration of sampling points according to the properties of the predicted solution $u(\mathbf{x}; \theta^1)$. Therefore, we construct the following monitor function.

$$\mathcal{W}(\mathbf{x}; \theta^1) = \frac{(\mathcal{R}(\mathbf{x}; \theta^1) + \mathcal{H}(\mathbf{x}; \theta^1))^s}{\int_{\Omega} (\mathcal{R}(\mathbf{x}; \theta^1) + \mathcal{H}(\mathbf{x}; \theta^1))^s d\mathbf{x}}, \quad (6)$$

where the exponent s is a positive parameter. A larger value of s leads to a higher concentration trend. Finally, the second-level residual training points $\mathcal{X}_{N_r}^2 = \{x_i\}_{i=1}^{N_r}$ can be sampled according to the density function $p(\mathbf{x}; \theta^1)$ of the monitoring function $\mathcal{W}(\mathbf{x}; \theta^1)$.

$$p(\mathbf{x}; \theta^1) \propto \mathcal{W}(\mathbf{x}; \theta^1) + c. \quad (7)$$

Where c is a penalty term constant, which ensures that even in regions where the monitoring function is small, a sufficient number of sampling points will still be obtained during sampling.

After the second-level training is completed, second-level sampling is needed to obtain third-level residual training points. Here, based on the predicted solution $\mathbf{u}(\mathbf{x}; \theta^2)$ obtained from the second-level training, the residuals in Eq (4) are updated.

$$\mathcal{R}(\mathbf{x}; (\theta^1, \theta^2)) = \left| \mathcal{A}[\mathbf{u}(\mathbf{x}; \theta^1) + \mathbf{u}(\mathbf{x}; \theta^2)] - f(\mathbf{x}) \right|. \quad (8)$$

Similarly, Eq (5) is also updated.

$$\mathcal{H}(\mathbf{x}; (\theta^1, \theta^2)) = \gamma |\nabla[\mathbf{u}(\mathbf{x}; \theta^1) + \mathbf{u}(\mathbf{x}; \theta^2)]|. \quad (9)$$

As mentioned above, the sampling method aims to make the sampling points more concentrated with increasing levels. Therefore, when constructing the new monitorfunction, the previous one isn't completely discarded but is included. Hence, the monitoring function for the second-level sampling is as shown below.

$$\begin{aligned} \mathcal{W}(\mathbf{x}; (\theta^1, \theta^2)) &= \mu \frac{[\mathcal{R}(\mathbf{x}; \theta^1) + \mathcal{H}(\mathbf{x}; \theta^1)]^s}{\int_{\Omega} [\mathcal{R}(\mathbf{x}; \theta^1) + \mathcal{H}(\mathbf{x}; \theta^1)]^s d\mathbf{x}} + \frac{[\mathcal{R}(\mathbf{x}; (\theta^1, \theta^2)) + \mathcal{H}(\mathbf{x}; (\theta^1, \theta^2))]^s}{\int_{\Omega} [\mathcal{R}(\mathbf{x}; (\theta^1, \theta^2)) + \mathcal{H}(\mathbf{x}; (\theta^1, \theta^2))]^s d\mathbf{x}} \\ &= \mu \mathcal{W}(\mathbf{x}; \theta^1) + \frac{[\mathcal{R}(\mathbf{x}; (\theta^1, \theta^2)) + \mathcal{H}(\mathbf{x}; (\theta^1, \theta^2))]^s}{\int_{\Omega} [\mathcal{R}(\mathbf{x}; (\theta^1, \theta^2)) + \mathcal{H}(\mathbf{x}; (\theta^1, \theta^2))]^s d\mathbf{x}}, \end{aligned} \quad (10)$$

where μ is a given positive constant. The presence of μ ensures that as the level increases, the points become more concentrated. Thus, the corresponding density function is obtained from the updated monitoring function to sample the third - level training points $\mathcal{X}_{N_r}^3 = \{x_i\}_{i=1}^{N_r}$.

$$p(\mathbf{x}; (\theta^1, \theta^2)) \propto \mathcal{W}(\mathbf{x}; (\theta^1, \theta^2)) + 1. \quad (11)$$

The details of the subsequent-level sampling will not be introduced one by one but will be summarized in Algorithm 1. For details on the parameter settings in the MLS method, please refer to Table 1.

3.1.2. Multi-level Training

In this section, we will elaborate on the training process within the Multi-Level framework. As is well known, the multi-grid method performs calculations on different grid levels, using coarse grids to address low-frequency errors and fine grids to tackle high-frequency errors, thereby effectively eliminating error components of all frequencies. Traditional iterative methods, such as the Jacobi and Gauss-Seidel iteration methods, are good at eliminating high - frequency errors but slow to attenuate low - frequency ones. Thus, the conventional multi - grid method starts with a fine grid, carries out several relaxation iterations (like the Gauss-Seidel iteration method) to eliminate high - frequency errors, and then transfers the remaining low - frequency errors to a coarse grid via a restriction operator for correction. However, in the process of solving PDEs with neural networks, the high-frequency parts of the solution are difficult to learn. So, our Multi-Level framework starts with uniformly sampled points for the first neural network training to eliminate low-frequency errors. Then, using the Multi-Level sampling, it leverages the neural network's generalization ability to transfer the remaining high-frequency errors onto new adaptive sampling points. Finally, it conducts the second training on these adaptive sampled points. In fact, this process is repeatable until the neural network effectively learns both the low-frequency and high-frequency information of the solution. Below, we'll start with the first level and go into the training process in detail.

The first - level training is straightforward. Sampling for the first - level training set is typically done via uniform sampling, which generally includes residual points $\mathcal{X}_{N_r}^1 = \{x_i\}_{i=1}^{N_r} \subset \Omega$ and boundary points $\mathcal{X}_{N_b} = \{x_i\}_{i=1}^{N_b} \subset \partial\Omega$.

Algorithm 1: Algorithm of Multi-level Sampling for the kth-level ($k > 2$).

1. Update the residual function:

$$\mathcal{R}(\mathbf{x}; (\theta^1, \theta^2, \dots, \theta^k)) = \left| \mathcal{A}[u(\mathbf{x}; \theta^1) + u(\mathbf{x}; \theta^2) + \dots + u(\mathbf{x}; \theta^k)] - f(\mathbf{x}) \right|.$$

2. Update the function with partial derivatives:

$$\mathcal{H}(\mathbf{x}; (\theta^1, \theta^2, \dots, \theta^k)) = \gamma |\nabla[u(\mathbf{x}; \theta^1) + u(\mathbf{x}; \theta^2) + \dots + u(\mathbf{x}; \theta^k)]|$$

3. Update the monitor function:

$$\begin{aligned} \mathcal{W}(\mathbf{x}; (\theta^1, \theta^2, \dots, \theta^k)) &= (k-1)\mu \frac{[\mathcal{R}(\mathbf{x}; \theta^1) + \mathcal{H}(\mathbf{x}; \theta^1)]^s}{\int_{\Omega} [\mathcal{R}(\mathbf{x}; \theta^1) + \mathcal{H}(\mathbf{x}; \theta^1)]^s d\mathbf{x}} + (k-2)\mu \frac{[\mathcal{R}(\mathbf{x}; (\theta^1, \theta^2)) + \mathcal{H}(\mathbf{x}; (\theta^1, \theta^2))]^s}{\int_{\Omega} [\mathcal{R}(\mathbf{x}; (\theta^1, \theta^2)) + \mathcal{H}(\mathbf{x}; (\theta^1, \theta^2))]^s d\mathbf{x}} \\ &+ \dots + \frac{[\mathcal{R}(\mathbf{x}; (\theta^1, \theta^2, \dots, \theta^k)) + \mathcal{H}(\mathbf{x}; (\theta^1, \theta^2, \dots, \theta^k))]^{\frac{1}{2}}}{\int_{\Omega} [\mathcal{R}(\mathbf{x}; (\theta^1, \theta^2, \dots, \theta^k)) + \mathcal{H}(\mathbf{x}; (\theta^1, \theta^2, \dots, \theta^k))]^{\frac{1}{2}} d\mathbf{x}} \\ &= \mu \mathcal{W}(\mathbf{x}; (\theta^1, \theta^2, \dots, \theta^{k-1})) + \frac{[\mathcal{R}(\mathbf{x}; (\theta^1, \theta^2, \dots, \theta^k)) + \mathcal{H}(\mathbf{x}; (\theta^1, \theta^2, \dots, \theta^k))]^{\frac{1}{2}}}{\int_{\Omega} [\mathcal{R}(\mathbf{x}; (\theta^1, \theta^2, \dots, \theta^k)) + \mathcal{H}(\mathbf{x}; (\theta^1, \theta^2, \dots, \theta^k))]^{\frac{1}{2}} d\mathbf{x}} \end{aligned}$$

4. Update the density function:

$$p(\mathbf{x}; (\theta^1, \theta^2, \dots, \theta^k)) \propto \mathcal{W}(\mathbf{x}; (\theta^1, \theta^2, \dots, \theta^k)) + 1.$$

5. Obtain the residual training points $\mathcal{X}_{N_r}^{k+1} = \{x_i\}_{i=1}^{N_r}$ for the k+1 level.

The deep solver aims to solve the general PDE system (Eq (1)). Once the training is complete, the deep solver's predicted solution is denoted as $u(\mathbf{x}; \theta^1)$.

Using the Multi-level sampling method, the residual training points $\mathcal{X}_{N_r}^2 = \{x_i\}_{i=1}^{N_r}$ for the second-level training can be obtained based on the first-level predicted solution $u(\mathbf{x}; \theta^1)$. Thus, when combined with the boundary training points, the second - level training points can be denoted as $\mathcal{X}_N^2 = \mathcal{X}_{N_r}^2 \cup \mathcal{X}_{N_b}$. Then, the more critical issue in the second - level training is determining the new objective of the deep solver. If the true solution of Eq (1) is denoted as $u^*(\mathbf{x})$, then the next goal is to make the deep solver learn $\mathbf{v}_1(\mathbf{x}; \theta^1) = u^*(\mathbf{x}) - u(\mathbf{x}; \theta^1)$. That is to say, in the second - level training, the deep solver needs to solve the following new partial differential equation.

$$\begin{cases} \mathcal{A}[u(\mathbf{x}; \theta^1) + \mathbf{v}_1(\mathbf{x}; \theta^1)] = f(\mathbf{x}), & \mathbf{x} \in \Omega \\ \mathcal{B}[u(\mathbf{x}; \theta^1) + \mathbf{v}_1(\mathbf{x}; \theta^1)] = g(\mathbf{x}). & \mathbf{x} \in \partial\Omega \end{cases} \quad (12)$$

Unlike multigrid methods that require restriction and interpolation operators to link computational results across different grids, the Multi-Level framework leverages the neural network's generalization ability. This allows it to provide predictions at new sampling points $u(\mathcal{X}_N^2; \theta^1)$, without introducing additional errors. Meanwhile, by combining automatic differentiation techniques, the partial derivative information about the first-level predicted solution at the second-level sampling points \mathcal{X}_N^2 can be obtained, such as $\nabla u(\mathcal{X}_N^2; \theta^1)$ and $\Delta u(\mathcal{X}_N^2; \theta^1)$. Depending on the specific forms of the partial differential operators \mathcal{A} and \mathcal{B} , the required parts can be filtered from the predicted solution $u(\mathcal{X}_N^2; \theta^1)$ and the partial derivative terms $\nabla u(\mathcal{X}_N^2; \theta^1)$ and $\Delta u(\mathcal{X}_N^2; \theta^1)$ to serve as new inputs. These new inputs, along with the second-level sampling points \mathcal{X}_N^2 , are fed into the deep solver for the second-level training. And this second-level training aims to learn $\mathbf{v}_1(\mathbf{x}; \theta^1)$ in order to solve Eq (12).

After the second-level training, we obtain the second-level predicted solution $u(\mathbf{x}; \theta^2)$. Similarly, if the sum of the predicted solutions from the first two layers is still not accurate enough, the target of the deep solver during the training of the third level should be $\mathbf{v}_2(\mathbf{x}; (\theta^1, \theta^2)) = u^*(\mathbf{x}) - u(\mathbf{x}; \theta^1) - u(\mathbf{x}; \theta^2)$. We skip detailed introduction of the third-level training, and summarize it into Algorithm 2 for the case of kth-level ($k > 2$).

Algorithm 2: Algorithm of Multi-level Training for the k th-level ($k > 2$).

1. Update the training points at the k th-level:

After completing the training at the $(k-1)$ th-level, use the Multi-level Sampling method to obtain the training points \mathcal{X}_N^k for the k th-level.

2. Update the predicted solutions and partial derivative terms at the k th-level:

Leveraging automatic differentiation and the generalization ability of neural networks, obtain $u(\mathcal{X}_N^k; \theta^{k-1})$, $\nabla u(\mathcal{X}_N^k; \theta^{k-1})$ and $\Delta u(\mathcal{X}_N^k; \theta^{k-1})$.

3. Solve the new partial differential equation at the k th-level

Let the deep solver aim to learn $\mathbf{v}_{k-1}(\mathbf{x}; (\theta^1, \theta^2, \dots, \theta^{k-1})) = \mathbf{u}^*(\mathbf{x}) - u(\mathbf{x}; \theta^1) - u(\mathbf{x}; \theta^2) - \dots - u(\mathbf{x}; \theta^{k-1})$ in solving the following equation.

$$\begin{cases} \mathcal{A}[u(\mathbf{x}; \theta^1) + u(\mathbf{x}; \theta^2) + \dots + \mathbf{v}_{k-1}(\mathbf{x}; (\theta^1, \theta^2, \dots, \theta^{k-1}))] = f(\mathbf{x}), & \mathbf{x} \in \Omega \\ \mathcal{B}[u(\mathbf{x}; \theta^1) + u(\mathbf{x}; \theta^2) + \dots + \mathbf{v}_{k-1}(\mathbf{x}; (\theta^1, \theta^2, \dots, \theta^{k-1}))] = g(\mathbf{x}). & \mathbf{x} \in \partial\Omega \end{cases} \quad (13)$$

4. Determine whether to perform training at the $(k+1)$ th-level.

3.1.3. Optimization methods

In deep learning solvers, optimization methods are crucial as they help in updating the model's parameters to minimize the loss function. They enable the model to learn from data and iteratively adjust parameters during training, working to reduce the error between the predicted and true solutions. In the selection of optimization methods for deep solvers, two approaches are most common. The first is the Adam method [9], which is a popular stochastic gradient descent approach. The Adam method represents a stochastic gradient descent variant that exhibits linear convergence. Its combination of momentum mechanisms and stochastic properties enables efficient escape from local minima and saddle points, which explains its widespread adoption during initial optimization phases. The second one is the LBFGS method [11], which is a quasi-Newton optimization approach. It determines the optimization direction by approximating the Hessian matrix and uses only limited memory to compute this approximation. Moreover, the superlinear convergence property of LBFGS enables it to find optimal parameters more rapidly than first - order methods. However, compared to the Adam method, it is more prone to getting stuck in the neighborhoods of saddle points. Therefore, the LBFGS method is often used as the second part of the optimization process for fine-tuning.

In this paper, we adopt two additional optimization methods, namely the SOAP method [19] and the SSBroyden method [1, 2, 18]. Although neither the SOAP method nor the SSBroyden method was first proposed in this paper, their combination seems not to have been attempted by other scholars before. SOAP (Shampoo with Adam in the Preconditioner's eigenbasis) is a novel deep learning optimization algorithm. It improves and stabilizes the Shampoo optimizer by incorporating the concept of the Adam optimizer, which runs Adam in the eigenbasis provided by Shampoo's preconditioner. SOAP combines Shampoo's higher-order preconditioning with Adam's adaptive learning rate mechanism. Specifically, during the k th training epoch, the steps of SOAP are mainly as follows:

- (i) Obtain the eigenvectors \mathbf{Q}_L and \mathbf{Q}_R of the preconditioners L_k and R_k from the shampoo algorithm.
- (ii) Project the gradient \mathbf{G}_k corresponding to the neural network parameters θ_k to the eigenspace:

$$\tilde{\mathbf{G}}_k = \mathbf{Q}_L^T \mathbf{G}_k \mathbf{Q}_R$$

- (iii) Update the parameters using the Adam algorithm:

$$\begin{cases} \widehat{Am}_k = \frac{\beta_1 \widehat{Am}_{k-1} + (1 - \beta_1) \widetilde{G}_k}{1 - \beta_1^k}, \\ \widehat{Av}_k = \frac{\beta_2 \widehat{Av}_{k-1} + (1 - \beta_2) \widetilde{G}_k^2}{1 - \beta_2^k}, \\ \widetilde{\theta}_{k+1} = \widetilde{\theta}_k - \eta_k \frac{\widehat{Am}_k}{\sqrt{\widehat{Av}_k + \epsilon}}, \end{cases}$$

where η_k represents the learning rate at the k th epoch, while β_1, β_2 and ϵ are hyperparameters.

(iv) Rotate the updated neural network parameters back to the original parameter space:

$$\theta_{k+1} = Q_L \widetilde{\theta}_{k+1} Q_R^T$$

Compared to Shampoo, SOAP reduces the number of hyperparameters and shows stronger robustness to changes in preconditioning frequency. Compared to Adam, it introduces only one extra hyperparameter (preconditioning frequency) but significantly cuts the required iterations and actual runtime.

Newton's method is a commonly - used optimization algorithm. It uses the gradient and Hessian matrix of a function to find the function's extreme value points. Its parameter update formula is as follows:

$$\theta_{k+1} = \theta_k - \eta_k \frac{G_k}{H_k^{-1}}$$

where H_k^{-1} is the inverse Hessian matrix of the loss function with parameter θ_k . However, explicitly calculating the inverse Hessian matrix is extremely costly in large-scale optimization problems. Instead, it's more common to approximate the inverse Hessian matrix. SSBroyden (self-scaled Broyden) method is a quasi-Newton iteration algorithm. It introduces the self-scaling factor τ_k and the updating parameter ϕ_k to improve the approximation of the inverse Hessian matrix. Specifically, the following formula is used for the update:

$$\begin{cases} \delta\theta_k = \theta_{k+1} - \theta_k, \\ \delta G_k = G_{k+1} - G_k, \\ \psi_k = \sqrt{\delta G_k \cdot H_k^{-1} \delta G_k} \left[\frac{\delta\theta_k}{\delta G_k \cdot \delta\theta_k} - \frac{H_k^{-1} \delta G_k}{\delta G_k \cdot H_k^{-1} \delta G_k} \right] \\ H_{k+1}^{-1} = \frac{1}{\tau_k} \left[H_k^{-1} - \frac{H_k^{-1} \delta G_k \otimes H_k^{-1} \delta G_k}{\delta G_k \cdot H_k^{-1} \delta G_k} + \phi_k \psi_k \otimes \psi_k \right] + \frac{\delta\theta_k \otimes \delta\theta_k}{\delta G_k \cdot \delta\theta_k}, \end{cases}$$

where \otimes is the tensor product. When $\tau_k = 1$ and $\phi_k = 1$, the SSBroyden algorithm reduces to the standard BFGS algorithm. For details on how τ_k and ϕ_k are updated, refer to [2]. Compared to the standard BFGS algorithm, by adjusting the self-scaling factor τ_k and update parameters τ_k , it can effectively control the condition number of the inverse Hessian matrix, improve the stability of the optimization process.

3.2. Error Estimation

Suppose that $\Omega \cup \partial\Omega = \bar{\Omega} \subset \mathbb{R}^d$ is compact. For a function $\mathbf{u} = [u_1, \dots, u_s]^T$ mapping from $\bar{\Omega} \rightarrow \mathbb{R}^s$, we define the following \mathbb{L}_2 norm:

$$\|\mathbf{u}\|_2 = \left[\sum_{i=1}^s \|u_i\|_2^2 \right]^{\frac{1}{2}}, \quad (14)$$

Multi-Level Deep Framework

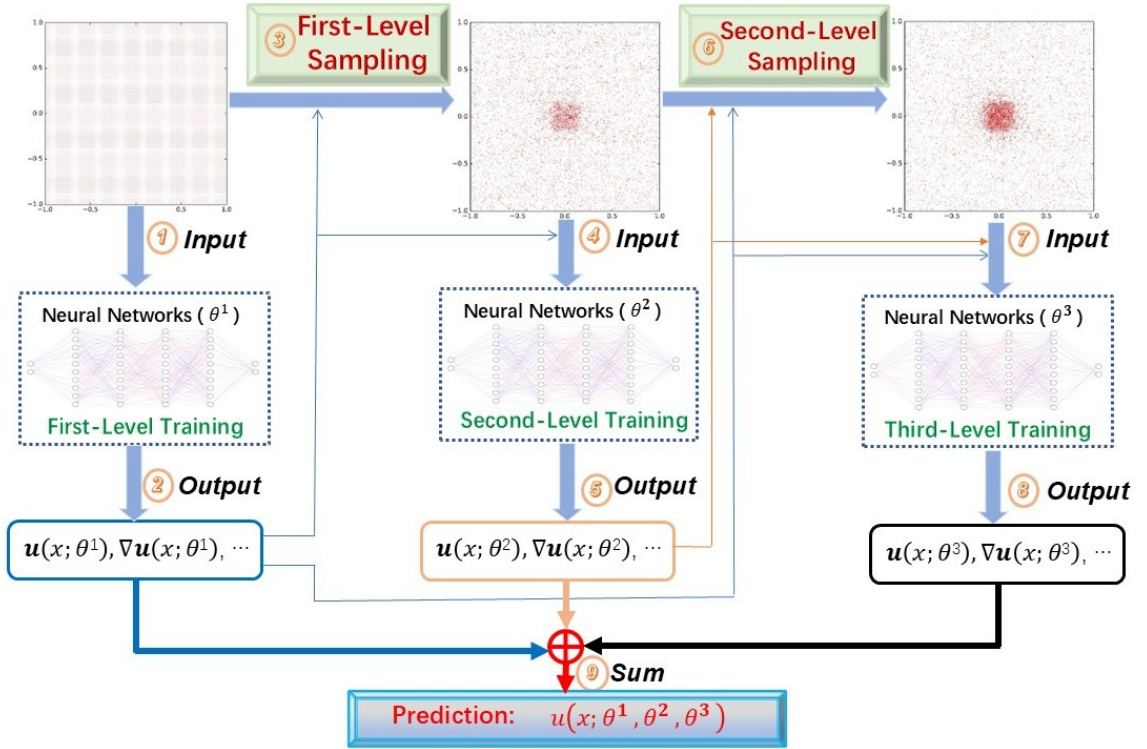


Figure 2: Flow chart of our framework.

where $\|u_i\|_2 = \left(\int_{\bar{\Omega}} |u_i(\mathbf{x})|^2 d\mathbf{x}\right)^{\frac{1}{2}}$. Then, we can define a Hilbert space \mathbb{H} consisting of $\mathbf{u} \in \mathbb{L}_2(\bar{\Omega})$, whose inner product is defined as:

$$\langle \mathbf{u}, \mathbf{v} \rangle = \sum_{i=1}^s \int_{\bar{\Omega}} u_i(\mathbf{x})v_i(\mathbf{x})d\mathbf{x}, \text{ where } \mathbf{u}, \mathbf{v} \in \mathbb{L}_2(\bar{\Omega}). \quad (15)$$

Now let the solution of Eq (1) be denoted as u^* , and let $u^* \in \mathbb{H}$, then we have the following theorem:

Theorem 1. For any $\mathbf{u}_1 \in \mathbb{H}$ and $\forall k \geq 2$, there exists a sequence of functions $\{\mathbf{u}_i\}_{i=1}^k \subset \mathbb{H}$ such that:

- (i) $\sum_{i=1}^k \mathbf{u}_i = u^*$;
- (ii) $\left\{ \left\| \sum_{i=1}^j \mathbf{u}_i - u^* \right\|_2 \right\}_{j=1}^k$ is a decreasing sequence.

Proof. $\forall \mathbf{u}_1 \in \mathbb{H}$ and $\forall k \geq 2$, the following sequence can be constructed.

$$\begin{cases} \mathbf{u}_1 = \mathbf{u}_1, \\ \mathbf{u}_i = \frac{(\mathbf{u}^* - \mathbf{u}_1)}{k-1}, 2 \leq i \leq k. \end{cases} \quad (16)$$

Then, it can be verified that the sequence $\{\mathbf{u}_i\}_{i=1}^k$ defined by Eq (16) satisfies Theorem 1.

Firstly, since \mathbb{H} is closed under scalar multiplication and addition, and $\mathbf{u}_1, u^* \in \mathbb{H}$, it follows that

$$\frac{(\mathbf{u}^* - \mathbf{u}_1)}{k-1} \in \mathbb{H}, 2 \leq i \leq k. \quad (17)$$

In other words, the sequence $\{\mathbf{u}_i\}_{i=1}^k$ is a subset of \mathbb{H} .

Secondly, it can be verified that the sequence defined by Eq (16) satisfies conclusion (i) in Theorem 1.

$$\sum_{i=1}^k \mathbf{u}_i = \mathbf{u}_1 + \sum_{i=2}^k \mathbf{u}_i = \mathbf{u}_1 + \sum_{i=2}^k \frac{(\mathbf{u}^* - \mathbf{u}_1)}{k-1} = \mathbf{u}_1 + \mathbf{u}^* - \mathbf{u}_1 = \mathbf{u}^*. \quad (18)$$

Finally, let $1 \leq j \leq k-1$, we have

$$\left\| \sum_{i=1}^j \mathbf{u}_i - \mathbf{u}^* \right\|_2 = \left\| \mathbf{u}_1 + \frac{j-1}{k-1}(\mathbf{u}^* - \mathbf{u}_1) - \mathbf{u}^* \right\|_2 = \left\| \frac{k-j}{k-1}(\mathbf{u}_1 - \mathbf{u}^*) \right\|_2 = \frac{k-j}{k-1} \|\mathbf{u}^* - \mathbf{u}_1\|_2. \quad (19)$$

Since $\left\{ \frac{k-j}{k-1} \right\}_{j=1}^k$ is a decreasing sequence, $\left\{ \left\| \sum_{i=1}^j \mathbf{u}_i - \mathbf{u}^* \right\|_2 \right\}_{j=1}^k$ is also a decreasing sequence. \square

It is worth mentioning that although Eq 16 in the proof of Theorem 1 provides one feasible form of the sequence that satisfies Theorem 1, it is evident that the sequence of functions satisfying Theorem 1 is not unique. Theorem 1's existence suggests that it's feasible to approximate solutions by seeking a finite number of functions within the solution space. However, when using PINNs to obtain predicted solutions, we must consider approximation errors. That is, we need to consider the situation where some functions in \mathbb{H} are not in the set of all predicted solutions output by deep neural networks.

Consider a fully connected neural network with an input layer of dimension d , an output layer of dimension s , a total of l_s layers, and the number of neurons per layer being $[m_1, m_2, \dots, m_{l_s}]$. The network has a nonlinear activation function σ , and the parameters of each layer consist of weights w and biases b . Let the set of predicted functions formed by the s outputs of the output layer be denoted as $\mathbf{u} = [u_1, \dots, u_s]$, and let this set be denoted as D_1^{NN} . Assuming $D_1^{NN} \subset \mathbb{H}$, then D_1^{NN} possesses the properties stated in Lemma 1.

Lemma 1. (i) (The existence of the zero element) $0 \in D_1^{NN}$.

(ii) (Closed under scalar multiplication) $\forall c \in \mathbb{R}$, if $\mathbf{u} \in D_1^{NN}$, then $c\mathbf{u} \in D_1^{NN}$.

Proof. Consider the i -th output u_i , $1 \leq i \leq s$ among the s outputs $[u_1, \dots, u_s]$ of the neural network, and focusing on the weights and biases from the last hidden layer to the output layer, we can express u_i in the following form.

$$u_i(\mathbf{x}) = \sum_{j=1}^{m_{l_s}} w_{i,j} \sigma(f_{l_s-1}(\mathbf{x})) + b_{i,j}, \quad 1 \leq i \leq s. \quad (20)$$

where $f_{l_s-1}(\mathbf{x})$ represents the information encoded by the neural network in the first $l_s - 1$ layers.

For each u_i , $1 \leq i \leq s$, if we set $w_{i,j} = b_{i,j} = 0$, $1 \leq j \leq m_{l_s}$, then $u_i(\mathbf{x}) = 0$, i.e., $\mathbf{u} = [u_1, \dots, u_s] = 0$. Thus, $0 \in D_1^{NN}$.

For each u_i , $1 \leq i \leq s$, $\forall c \in \mathbb{R}$, let $\hat{w}_{i,j} = cw_{i,j}$ and $\hat{b}_{i,j} = cb_{i,j}$. Denote \hat{u}_i , $1 \leq i \leq s$ as the following equation.

$$\hat{u}_i(\mathbf{x}) = \sum_{j=1}^{m_{l_s}} \hat{w}_{i,j} \sigma(f_{l_s-1}(\mathbf{x})) + \hat{b}_{i,j}, \quad 1 \leq i \leq s. \quad (21)$$

Obviously, if $\mathbf{u} = [u_1, \dots, u_s] \in D_1^{NN}$, then $\hat{\mathbf{u}} = [\hat{u}_1, \dots, \hat{u}_s] \in D_1^{NN}$, $1 \leq i \leq s$. Thus, $c\mathbf{u} \in D_1^{NN}$ \square

Definition 1. Suppose D is a subset of \mathbb{H} and $\mathbf{u}^* \in \mathbb{H}$, the distance between D and \mathbf{u}^* is given below.

$$d(D, \mathbf{u}^*) = \inf \{ \|\mathbf{u} - \mathbf{u}^*\|_2, \forall \mathbf{u} \in D \} \quad (22)$$

If there exists some $\mathbf{u} \in D$ such that $d(D, \mathbf{u}^*) = \|\mathbf{u} - \mathbf{u}^*\|_2$, then \mathbf{u} is called the optimal approximation of \mathbf{u}^* in D .

In our framework, when $k = 2$, after fixing $\forall \mathbf{u}_1 \in D_1^{NN}$, we look for an element \mathbf{u}_2 in D_1^{NN} such that $\mathbf{u}_1 + \mathbf{u}_2$ approximates \mathbf{u}^* . This is equivalent to finding an element in the new set $D_2^{NN} = \{\mathbf{u}_1 + \mathbf{u}_2 | \forall \mathbf{u}_2 \in D_1^{NN}\}$ to approximate \mathbf{u}^* .

Definition 2. When $k \geq 3$, suppose \mathbf{u}_{k-1}^{opt} is the optimal approximation of \mathbf{u}^* in D_{k-1}^{NN} , the following definition of D_k^{NN} can be given.

$$D_k^{NN} = \left\{ \mathbf{u} + \mathbf{u}_{k-1}^{opt} | \forall \mathbf{u} \in D_1^{NN} \right\} \quad (23)$$

In the following assumption, only the approximation error arising from the representational capacity of the neural network is considered, without accounting for errors introduced by the discretization of integrals or optimization methods.

Assumption 1. For any $k \geq 2$, the optimization method finds the optimal approximation \mathbf{u}_k^{opt} of \mathbf{u}^* in D_k^{NN} and $\|\mathbf{u}_k^{opt} - \mathbf{u}^*\|_2 > 0$.

Theorem 2. For any $\mathbf{u}_1 \in D_1^{NN}$ and $\forall k \geq 2$, under Assumption 1, there exists a sequence of functions $\{\mathbf{u}_i\}_{i=1}^k \subset D_1^{NN}$ such that:

- (i) $\left\{ \left\| \sum_{i=1}^j \mathbf{u}_i - \mathbf{u}^* \right\|_2 \right\}_{j=1}^k$ is a decreasing sequence;
- (ii) If $\forall \mathbf{u} \in \{\mathbf{u}_i\}_{i=2}^k$, $\mathbf{u} \neq 0$, then $\left\{ \left\| \sum_{i=1}^j \mathbf{u}_i - \mathbf{u}^* \right\|_2 \right\}_{j=1}^k$ is a strictly decreasing sequence.

Proof. $\forall \mathbf{u}_1 \in D_1^{NN}$ and $\forall k \geq 2$, the following sequence can be constructed.

$$\begin{cases} \mathbf{u}_1 = \mathbf{u}_1, \\ \mathbf{u}_2 = \mathbf{u}_2^{opt} - \mathbf{u}_1, \\ \mathbf{u}_i = \mathbf{u}_i^{opt} - \mathbf{u}_{i-1}^{opt}, 3 \leq i \leq k \end{cases} \quad (24)$$

Then, it can be verified that the sequence $\{\mathbf{u}_i\}_{i=1}^k$ defined by Eq (24) satisfies Theorem 2.

Firstly, for each \mathbf{u}_i , $3 \leq i \leq k$, according to Definition 2, we have

$$\exists \mathbf{u} \in D_1^{NN}, \text{ s.t.}, \mathbf{u}_{i-1}^{opt} + \mathbf{u} = \mathbf{u}_i^{opt} \in D_i^{NN}, 3 \leq i \leq k. \quad (25)$$

So $\forall \mathbf{u}_i \in D_1^{NN}$, $3 \leq i \leq k$. Similarly, according to the definition of D_2^{NN} , there is $\mathbf{u}_2 \in D_1^{NN}$. Hence, the sequence $\{\mathbf{u}_i\}_{i=1}^k \subset D_1^{NN}$.

Secondly, according to Eq (24), to prove conclusion (i), it suffices to show that

$$\left\{ \|\mathbf{u}_1 - \mathbf{u}^*\|_2, \|\mathbf{u}_2^{opt} - \mathbf{u}^*\|_2, \dots, \|\mathbf{u}_k^{opt} - \mathbf{u}^*\|_2 \right\}$$

is a decreasing sequence. We will prove that, for $3 \leq i \leq k$, $\|\mathbf{u}_{i-1}^{opt} - \mathbf{u}^*\|_2 \leq \|\mathbf{u}_i^{opt} - \mathbf{u}^*\|_2$. Based on the definition of \mathbf{u}_i^{opt} , there is

$$\forall \mathbf{u} \in D_i^{NN}, \text{ s.t.}, \|\mathbf{u} - \mathbf{u}^*\|_2 \geq \|\mathbf{u}_i^{opt} - \mathbf{u}^*\|_2. \quad (26)$$

According to Lemma 1, $0 \in D_1^{NN}$, which means $\mathbf{u}_{i-1}^{opt} + 0 = \mathbf{u}_i^{opt} \in D_i^{NN}$. Based on Equation 3, we can draw the following conclusion.

$$\|\mathbf{u}_{i-1}^{opt} - \mathbf{u}^*\|_2 \geq \|\mathbf{u}_i^{opt} - \mathbf{u}^*\|_2, 3 \leq i \leq k. \quad (27)$$

Similarly, it can also be proved that $\|\mathbf{u}_1 - \mathbf{u}^*\|_2 \geq \|\mathbf{u}_2^{opt} - \mathbf{u}^*\|_2$. Thus, $\left\{ \|\mathbf{u}_1 - \mathbf{u}^*\|_2, \|\mathbf{u}_2^{opt} - \mathbf{u}^*\|_2, \dots, \|\mathbf{u}_k^{opt} - \mathbf{u}^*\|_2 \right\}$ is a decreasing sequence.

Finally, according to Eq (24), to prove conclusion (ii), it suffices to prove that if $\forall \mathbf{u} \in \{\mathbf{u}_i\}_{i=2}^k, \mathbf{u} \neq 0$,

$$\left\{ \|\mathbf{u}_1 - \mathbf{u}^*\|_2, \|\mathbf{u}_2^{opt} - \mathbf{u}^*\|_2, \dots, \|\mathbf{u}_k^{opt} - \mathbf{u}^*\|_2 \right\}$$

is a strictly decreasing sequence. Still, first consider the case where $3 \leq i \leq k$. Based on Eq (24), we have

$$\|\mathbf{u}_{i-1}^{opt} - \mathbf{u}^*\|_2 = \|\mathbf{u}_i^{opt} - \mathbf{u}_i - \mathbf{u}^*\|_2 \quad (28)$$

Take the square and apply the inner product, then we have

$$\begin{aligned} \|\mathbf{u}_{i-1}^{opt} - \mathbf{u}^*\|_2^2 &= \|\mathbf{u}_i^{opt} - \mathbf{u}_i - \mathbf{u}^*\|_2^2 = \|\mathbf{u}_i^{opt} - \mathbf{u}^*\|_2^2 + \|\mathbf{u}_i\|_2^2 + 2\langle \mathbf{u}_i^{opt} - \mathbf{u}^*, -\mathbf{u}_i \rangle \\ &= \|\mathbf{u}_i^{opt} - \mathbf{u}^*\|_2^2 + \|\mathbf{u}_i\|_2^2 + 2\langle \mathbf{u}_i^{opt} - \mathbf{u}^*, \mathbf{u}_{i-1}^{opt} - \mathbf{u}_i^{opt} \rangle \end{aligned} \quad (29)$$

Since $\forall \mathbf{u} \in \{\mathbf{u}_i\}_{i=2}^k, \mathbf{u} \neq 0$, there is

$$\|\mathbf{u}_{i-1}^{opt} - \mathbf{u}^*\|_2^2 > \|\mathbf{u}_i^{opt} - \mathbf{u}^*\|_2^2 + 2\langle \mathbf{u}_i^{opt} - \mathbf{u}^*, \mathbf{u}_{i-1}^{opt} - \mathbf{u}_i^{opt} \rangle \quad (30)$$

Next, we only need to prove that $\langle \mathbf{u}_i^{opt} - \mathbf{u}^*, \mathbf{u}_{i-1}^{opt} - \mathbf{u}_i^{opt} \rangle \geq 0$.

Using proof by contradiction, suppose $\langle \mathbf{u}_i^{opt} - \mathbf{u}^*, \mathbf{u}_{i-1}^{opt} - \mathbf{u}_i^{opt} \rangle < 0$. According to Lemma 1, if $\mathbf{u}_i \in D_1^{NN}, \forall \lambda \in \mathbb{R}$, then $(1 - \lambda)\mathbf{u}_i \in D_1^{NN}$. So we have

$$\begin{aligned} \mathbf{u}_i^{NN} &:= \mathbf{u}_i^{opt} + \lambda(\mathbf{u}_{i-1}^{opt} - \mathbf{u}_i^{opt}) = \lambda\mathbf{u}_{i-1}^{opt} + (1 - \lambda)\mathbf{u}_i^{opt} \\ &= \mathbf{u}_{i-1}^{opt} + (1 - \lambda)(\mathbf{u}_i^{opt} - \mathbf{u}_{i-1}^{opt}) \\ &= \mathbf{u}_{i-1}^{opt} + (1 - \lambda)\mathbf{u}_i \in D_1^{NN} \end{aligned} \quad (31)$$

Then, we have

$$\begin{aligned} \|\mathbf{u}^* - \mathbf{u}_i^{NN}\|_2^2 &= \|\mathbf{u}^* - \mathbf{u}_{i-1}^{opt} - \lambda(\mathbf{u}_{i-1}^{opt} - \mathbf{u}_i^{opt})\|_2^2 \\ &= \|\mathbf{u}^* - \mathbf{u}_{i-1}^{opt}\|_2^2 - 2\lambda\langle \mathbf{u}^* - \mathbf{u}_{i-1}^{opt}, \mathbf{u}_{i-1}^{opt} - \mathbf{u}_i^{opt} \rangle + \lambda^2\|\mathbf{u}_{i-1}^{opt} - \mathbf{u}_i^{opt}\|_2^2 \end{aligned} \quad (32)$$

Since $\langle \mathbf{u}_i^{opt} - \mathbf{u}^*, \mathbf{u}_{i-1}^{opt} - \mathbf{u}_i^{opt} \rangle < 0$, there is $\langle \mathbf{u}^* - \mathbf{u}_{i-1}^{opt}, \mathbf{u}_{i-1}^{opt} - \mathbf{u}_i^{opt} \rangle > 0$.

Then, $\exists \lambda$ satisfy $0 < \lambda < \frac{2\langle \mathbf{u}^* - \mathbf{u}_{i-1}^{opt}, \mathbf{u}_{i-1}^{opt} - \mathbf{u}_i^{opt} \rangle}{\|\mathbf{u}_{i-1}^{opt} - \mathbf{u}_i^{opt}\|_2^2}$ such that

$$-2\lambda\langle \mathbf{u}^* - \mathbf{u}_{i-1}^{opt}, \mathbf{u}_{i-1}^{opt} - \mathbf{u}_i^{opt} \rangle + \lambda^2\|\mathbf{u}_{i-1}^{opt} - \mathbf{u}_i^{opt}\|_2^2 < 0 \quad (33)$$

Based on Eq (32) and (33), there is

$$\|\mathbf{u}^* - \mathbf{u}_i^{NN}\|_2^2 < \|\mathbf{u}^* - \mathbf{u}_{i-1}^{opt}\|_2^2 \quad (34)$$

It is evident that Eq (34) contradicts the definition of \mathbf{u}_i^{opt} . So, there is $\langle \mathbf{u}_i^{opt} - \mathbf{u}^*, \mathbf{u}_{i-1}^{opt} - \mathbf{u}_i^{opt} \rangle \geq 0$. Thus, we complete the proof for $3 \leq i \leq k$. As for the case $i = 2$, replacing \mathbf{u}_{i-1}^{opt} with \mathbf{u}_1 in the above proof yields the same conclusion. \square

Assumption 2. Let $\forall \mathbf{u} \in \mathbb{H}$, the following assumption holds

$$C_1\|\mathbf{u}\|_2 \leq \|\mathcal{A}(\mathbf{u})\|_2 + \|\mathcal{B}(\mathbf{u})\|_2 \leq C_2\|\mathbf{u}\|_2, \quad (35)$$

where C_1 and C_2 are positive constants.

In order to give an upper bound of the error, we need to introduce the the Rademacher complexity.

Definition 3. Let $\mathcal{X} := \{x_i\}_{i=1}^n$ be a collection of i.i.d. random samples, the Rademacher complexity of the function class \mathcal{F} can be defined as

$$\mathcal{R}_n(\mathcal{F}) = \mathbb{E}_{\mathcal{X}, \epsilon} \left(\sup_{f \in \mathcal{F}} \left| \frac{1}{n} \sum_{i=1}^n \epsilon_i f(x_i) \right| \right),$$

where $(\epsilon_1, \epsilon_2, \dots, \epsilon_n)$ are i.i.d. Rademacher variables, i.e., $P(\epsilon_i = 1) = P(\epsilon_i = -1) = 0.5$.

Now we consider the approximate solution in the set $\mathcal{F}_k^{NN}(\mathbf{u}_1, \dots, \mathbf{u}_{k-1}) = \left\{ \mathbf{u}_k + \sum_{i=1}^{k-1} \mathbf{u}_i \mid \forall \mathbf{u}_k \in D_1^{NN} \right\}$.

Assumption 3. $\forall \mathbf{u} \in \mathcal{F}_k^{NN}(\mathbf{u}_1, \dots, \mathbf{u}_{k-1})$, there exists a positive number $0 < B_r \in \mathbb{R}$ such that

$$\begin{aligned} \sup \|\mathcal{A}[\mathbf{u}(\mathbf{x})] - f(\mathbf{x})\|_{\infty} &= B_r, \\ \sup \|\mathcal{B}[\mathbf{u}(\mathbf{x})] - g(\mathbf{x})\|_{\infty} &= B_g. \end{aligned} \quad (36)$$

According to [20], we use Lemma 2 and propose the following theorem about the Rademacher complexity.

Lemma 2. Let \mathcal{F} be a b -uniformly bounded class of integrable real-valued functions with domain Ω , for any positive integer $n \geq 1$ and any scalar $\delta \geq 0$, we have

$$\sup_{f \in \mathcal{F}} \left| \frac{1}{n} \sum_{i=1}^n f(x_i) - \mathbb{E}[f(x)] \right| \leq 2\mathcal{R}_n(\mathcal{F}) + \delta,$$

with probability at least $1 - \exp\left(-\frac{n\delta^2}{2b^2}\right)$.

Theorem 3. Suppose that Assumption 2 and Assumption 3 hold, let \mathbf{u}^* be the exact solution of Eq (1). $\forall \delta > 0$, $\{x_i\}_{i=1}^{M_r}$ is a collection of i.i.d. random samples and $\forall \mathbf{u}(\mathbf{x}; \theta) \in \mathcal{F}_k^{NN}(\mathbf{u}_1, \dots, \mathbf{u}_{k-1})$, the following error estimate holds

$$\|\mathbf{u}^*(\mathbf{x}) - \mathbf{u}(\mathbf{x}; \theta)\|_2 \leq \frac{\sqrt{2}}{C_1} \left(\|r(\mathbf{x}; \theta)\|_{2, N_r}^2 + \|b(\mathbf{x}; \theta)\|_{2, N_b}^2 + 2\mathcal{R}_{N_r}(\mathcal{F}_k^{NN}(\mathbf{u}_1, \dots, \mathbf{u}_{k-1})) + 2\mathcal{R}_{N_b}(\mathcal{F}_k^{NN}(\mathbf{u}_1, \dots, \mathbf{u}_{k-1})) + \delta \right)^{\frac{1}{2}}, \quad (37)$$

with probability at least $\left(1 - \exp\left(-\frac{N_r \delta^2}{8B_r^2}\right)\right) \left(1 - \exp\left(-\frac{N_b \delta^2}{8B_g^2}\right)\right)$.

Proof. By Assumption 2, we have

$$\begin{aligned} C_1 \|\mathbf{u}^*(\mathbf{x}) - \mathbf{u}(\mathbf{x}; \theta)\|_2 &\leq \|\mathcal{A}(\mathbf{u}^*(\mathbf{x})) - \mathcal{A}(\mathbf{u}(\mathbf{x}; \theta))\|_2 + \|\mathcal{B}(\mathbf{u}^*(\mathbf{x})) - \mathcal{B}(\mathbf{u}(\mathbf{x}; \theta))\|_2 \\ &= \|\mathcal{A}(\mathbf{u}(\mathbf{x}; \theta)) - f\|_2 + \|\mathcal{B}(\mathbf{u}(\mathbf{x}; \theta)) - g\|_2 \\ &= \|r(\mathbf{x}; \theta)\|_2 + \|b(\mathbf{x}; \theta)\|_2 \\ &\leq \sqrt{2} \left(\|r(\mathbf{x}; \theta)\|_2^2 + \|b(\mathbf{x}; \theta)\|_2^2 \right)^{\frac{1}{2}}. \end{aligned} \quad (38)$$

Using Lemma 2, we have

$$\|r(\mathbf{x}; \theta)\|_2^2 \leq \|r(\mathbf{x}; \theta)\|_{2, N_r}^2 + 2\mathcal{R}_{N_r}(\mathcal{F}_k^{NN}(\mathbf{u}_1, \dots, \mathbf{u}_{k-1})) + \frac{\delta}{2}, \quad (39)$$

with probability at least $1 - \exp\left(-\frac{N_r \delta^2}{8B_r^2}\right)$.

$$\|b(\mathbf{x}; \theta)\|_2^2 \leq \|b(\mathbf{x}; \theta)\|_{2, N_b}^2 + 2\mathcal{R}_{N_b}(\mathcal{F}_k^{NN}(\mathbf{u}_1, \dots, \mathbf{u}_{k-1})) + \frac{\delta}{2}, \quad (40)$$

Table 1

Default settings for main parameters in MLS method.

γ	s	c	μ
1	0.5	1	4

Table 2

Default settings for main parameters in PINNs.

Torch Version	Activation Function	Initialization Method Rate	Loss Weights (α_1 / α_2)	Net Size	Random Seed
2.4.0	Tanh	Xavier	1/1	40 × 4	100

with probability at least $1 - \exp\left(-\frac{N_b \delta^2}{8B_g^2}\right)$.

Therefore,

$$\begin{aligned} \|\mathbf{u}^*(\mathbf{x}) - \mathbf{u}(\mathbf{x}; \theta)\|_2 &\leq \frac{\sqrt{2}}{C_1} (\|r(\mathbf{x}; \theta)\|_2^2 + \|b(\mathbf{x}; \theta)\|_2^2)^{\frac{1}{2}} \\ &\leq \frac{\sqrt{2}}{C_1} \left(\|r(\mathbf{x}; \theta)\|_{2, N_r}^2 + \|b(\mathbf{x}; \theta)\|_{2, N_b}^2 + 2\mathcal{R}_{N_r}(\mathcal{F}_k^{NN}(\mathbf{u}_1, \dots, \mathbf{u}_{k-1})) + 2\mathcal{R}_{N_b}(\mathcal{F}_k^{NN}(\mathbf{u}_1, \dots, \mathbf{u}_{k-1})) + \delta \right)^{\frac{1}{2}}, \end{aligned} \quad (41)$$

with probability at least $\left(1 - \exp\left(-\frac{N_r \delta^2}{8B_r^2}\right)\right) \left(1 - \exp\left(-\frac{N_b \delta^2}{8B_g^2}\right)\right)$. \square

4. Numerical Experiments

4.1. Symbols and parameter settings

Let the exact solution be denote as \mathbf{u}^* , and the approximate solution be denote as $\mathbf{u}(\mathbf{x}; \theta)$. The relative errors in the test set $\{\mathbf{x}_i\}_{i=1}^{M_t}$ are defined as follows

$$\begin{aligned} e_\infty(\mathbf{u}) &= \frac{\max_{1 \leq i \leq M_t} |\mathbf{u}^*(x_i) - \mathbf{u}(x_i; \theta)|}{\max_{1 \leq i \leq M_t} |\mathbf{u}^*(x_i)|}, \\ e_2(\mathbf{u}) &= \frac{\sqrt{\sum_{i=1}^{M_t} |\mathbf{u}^*(x_i) - \mathbf{u}(x_i; \theta)|^2}}{\sqrt{\sum_{i=1}^{M_t} |\mathbf{u}^*(x_i)|^2}}. \end{aligned} \quad (42)$$

In order to reduce the effect of randomness on the calculation results, we set all the seeds of the random numbers to 100. The default parameter settings in MLS method and PINNs are given in Table (1 and 2). All numerical simulations are carried on NVIDIA A100 with 80GB of memory and NVIDIA A800 with 80GB of memory.

4.2. One-dimensional Advection-Diffusion equation

Considering the following one-dimensional convection-diffusion equation

$$\begin{cases} -cu'' + bu' = f(x), & (x, y) \text{ in } \Omega, \\ u(x, y) = 0, & (x, y) \text{ on } \partial\Omega, \end{cases} \quad (43)$$

where $\Omega = (-1, 1)$. When $f(x) \equiv 1$, the solution to this problem is given by

$$u = \frac{x}{b} + \frac{1}{b} \left(\frac{e^{-\frac{2b}{c}+1}}{e^{-\frac{2b}{c}}-1} \right) \left(\frac{2e^{\frac{b}{c}(x-1)}}{e^{-\frac{2b}{c}}+1} - 1 \right). \quad (44)$$

When the value of ϵ is small, it is difficult to solve the boundary layer accurately. Therefore, we set $\epsilon = 0.01$ and $b = -1$.

In this experiment, we sample 200 points within Ω as the residual training set, and we employ a three-level framework for training. In the first-level pre-training, we trained 5000 epochs using the SOAP method. Then, in the second-level training, we again trained 5000 epochs of the SOAP method and 3000 epochs of the SSB method. Finally, in the third-level training, we employed 3300 epochs of the SSB method.

During training at the different levels, we employed the MLS method described in Section 3.1.1. Fig 3 illustrates the effect of the MLS method across the various levels; it can be seen that as the level increases, the points progressively concentrate toward $x = -1$, because the solution has very low regularity in the vicinity of $x = -1$. It can be seen that the MLS method is able to capture this property effectively.

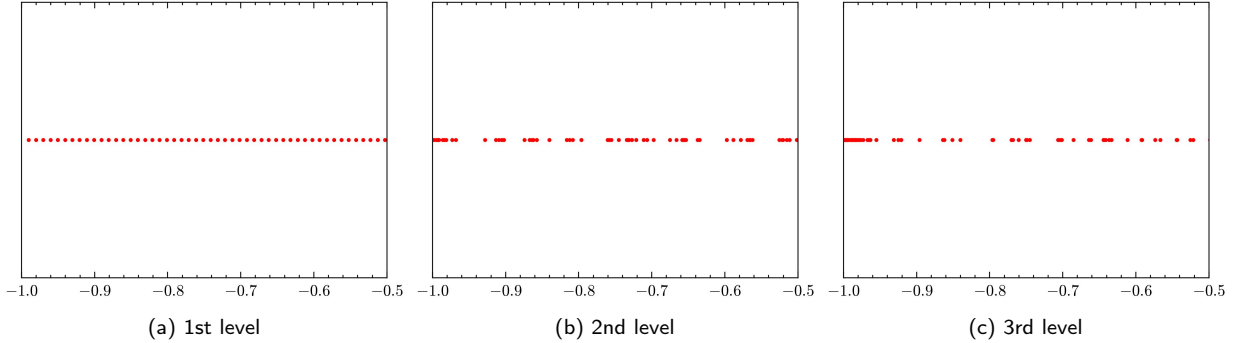


Figure 3: The sampling points at different levels for the one-dimensional advection-diffusion equation with the solution Eq (44). This figure shows the behavior of sampling points in $[-1, -0.5]$.

The numerical results of different levels are given in Fig 4. Fig 4 illustrates figures based on the predicted solutions $\mathbf{u}(\mathbf{x}; \theta)$ and the absolute error $|\mathbf{u}^*(\mathbf{x}) - \mathbf{u}(\mathbf{x}; \theta)|$. It can be observed that as the level increases, the approximation error decreases, demonstrating the effectiveness of our multi-level deep framework.

In Fig 5, we compare the commonly used RAD method in PINNs under the same number of training epochs. Specifically, the training process consists of pre-training with 5000 iterations of Adam optimizer, followed by sampling with the RAD method, finally trains again for 5000 Adam epochs and 6300 L-BFGS epochs. Fig 5 illustrates the variation of the relative errors during the training process, from which the superiority of our method can be observed. In the subsequent experiments, we will conduct a more detailed comparison on more complex cases. Ultimately, the relative errors of our method in solving the one-dimensional advection-diffusion equation with the solution Eq (44) are $e_\infty(\mathbf{u}) = 1.561 \times 10^{-7}$ and $e_2(\mathbf{u}) = 5.494 \times 10^{-8}$.

4.3. Two-dimensional Poisson equation

For the following Poisson equation in two-dimension

$$\begin{cases} -\Delta u(x, y) = f(x, y), & (x, y) \text{ in } \Omega, \\ u(x, y) = g(x, y), & (x, y) \text{ on } \partial\Omega, \end{cases} \quad (45)$$

where $\Omega = (-1, 1)^2$, the exact solution which has a peak at $(0, 0)$ is chosen as

$$\mathbf{u} = e^{-1000(x^2+y^2)}. \quad (46)$$

The Dirichlet boundary condition $g(x, y)$ and the source function $f(x, y)$ are given by Eq (46).

In this experiment, we sample 10000 points within Ω as the residual training set and 1000 points on $\partial\Omega$ as the boundary training set, while utilizing 400×400 points for the test set, and we employ a four-level framework for training. In the first-level pre-training, we trained 20000 epochs using the SOAP method and 10000 epochs using the SSB method. In the second-level training, we again trained 20000 epochs of the SOAP method and 10000 epochs of the SSB method. In the third-level training, we employed 5000 epochs of the SSB method. Finally, in the fourth-level training, we used 10000 epochs of the SSB method.

Multi-Level Deep Framework

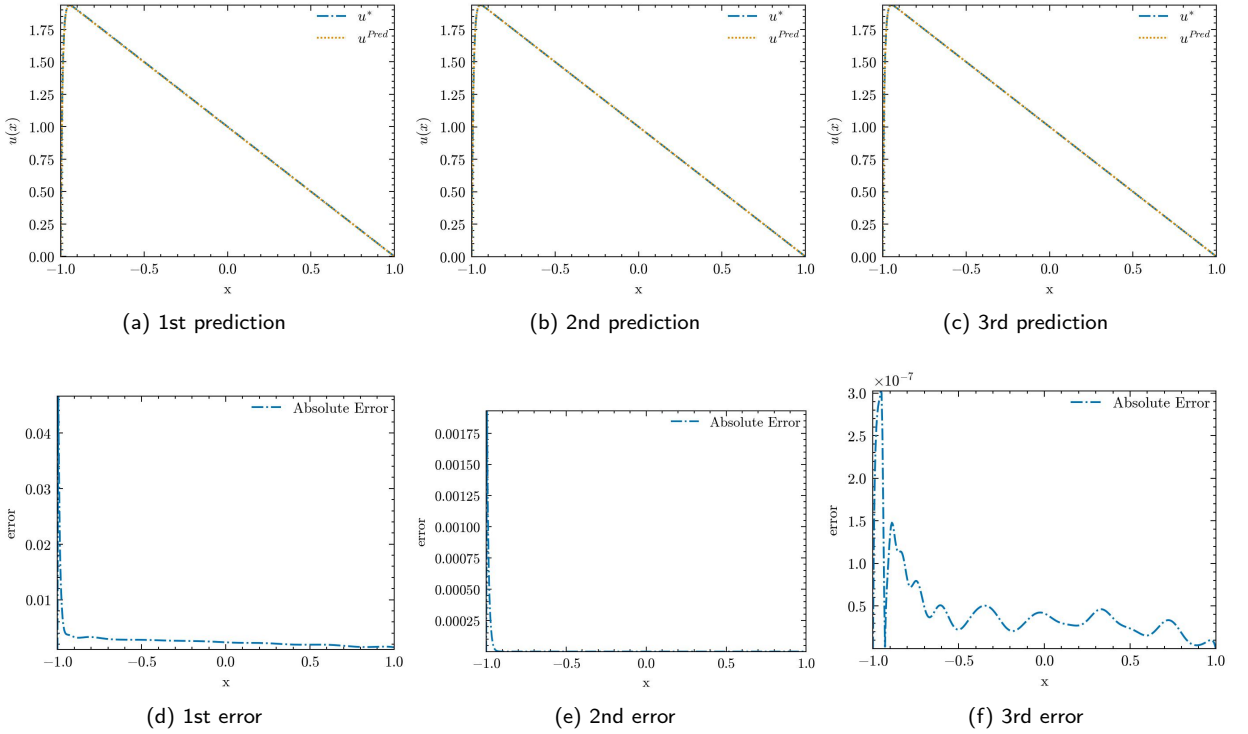


Figure 4: The numerical result of different levels for the one-dimensional advection-diffusion equation with the solution Eq (44). (a)–(c) Comparison between the predicted $\mathbf{u}(\mathbf{x}; \theta)$ and exact solutions $\mathbf{u}^*(\mathbf{x})$. (d)–(f) Performance of the absolute error $|\mathbf{u}^*(\mathbf{x}) - \mathbf{u}(\mathbf{x}; \theta)|$.

During training at the different levels, we employed the MLS method described in Section 3.1.1. Fig 7 illustrates the effect of the MLS method across the various levels; it can be seen that as the level increases, the points progressively concentrate toward the origin, because the solution has very low regularity in the vicinity of the origin. It can be seen that the MLS method is able to capture this property effectively.

The numerical results of different levels are given in Fig 8. Fig 8 illustrates heat-maps based on absolute error $|\mathbf{u}^*(\mathbf{x}) - \mathbf{u}(\mathbf{x}; \theta)|$. It can be observed that as the level increases, the approximation error decreases, demonstrating the effectiveness of our multi-level framework.

To further highlight the advantages of our approach, we compare it here with three alternative strategies.

- Strategy 1 employs the widely-used RAD-PINN method: it pre-trains for 20000 Adam epochs and 10000 L-BFGS epochs, then performs RAD adaptive sampling, and finally trains again for 20000 Adam epochs and 20000 L-BFGS epochs.
- Strategy 2 uses the MLT method but dispenses with adaptive sampling: it pre-trains for 20000 Soap epochs and 10000 SSB epochs, then continues with a second-level training of 20000 Soap epochs and 10000 SSB epochs, followed by a third-level training of 5000 SSB epochs and a fourth-level training of another 5000 SSB epochs.
- Strategy 3 optimizes with Soap and SSB while still following the RAD-PINN pipeline: it pre-trains for 20000 Soap epochs and 10000 SSB epochs, carries out RAD adaptive sampling, and afterward trains for 20000 Soap epochs and 20000 SSB epochs.
- Strategy 4 is the multilevel framework that combines the MLS and MLT methods: it pre-trains for 20000 Soap epochs and 10000 SSB epochs, uses MLS method to generate second-level sampling points and trains at that level for 20000 Soap epochs and 10000 SSB epochs, then uses MLS method to obtain third-level points and trains for 5000 SSB epochs, and finally uses MLS method to obtain fourth-level points and trains for another 5000 SSB epochs.

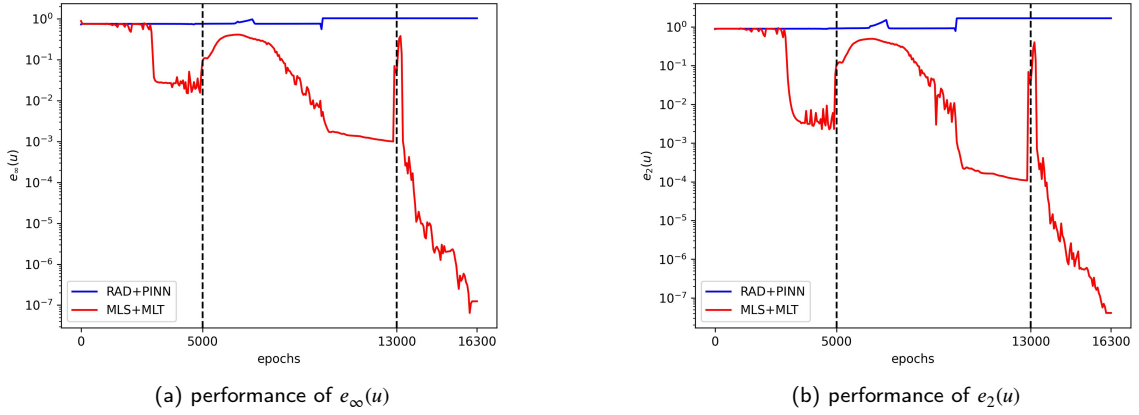


Figure 5: The performance of errors for the one-dimensional advection-diffusion equation with the solution Eq (44). (a) the relative error $e_\infty(u)$ with different training epochs; (b) the relative error $e_2(u)$ with different training epochs.

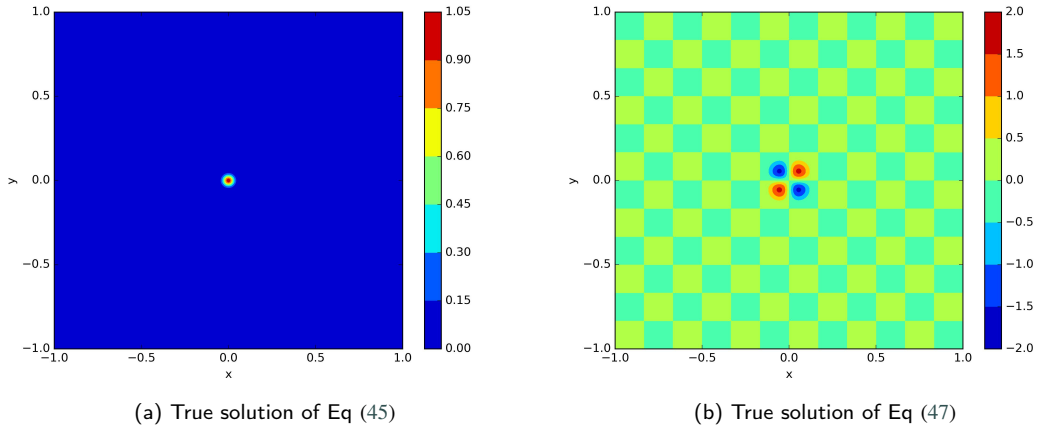


Figure 6: Here are the heatmaps of the true solutions Eq (46) and Eq (48).

Table 3

Comparison of errors using different methods for two-dimensional Poisson equation with one peak of Eq (46).

Relative error	Strategy 1	Strategy 2	Strategy 3	Strategy 4
$e_\infty(u)$	3.656×10^{-3}	1.857×10^{-3}	5.811×10^{-6}	7.033×10^{-7}
$e_2(u)$	6.810×10^{-2}	4.744×10^{-3}	4.266×10^{-3}	8.285×10^{-6}

Fig 9 shows the performance of these four strategies across training epochs. By comparing Strategy 1 with Strategy 4, we can demonstrate the advantages of our method over the standard RAD-PINN; by comparing Strategy 1 with Strategy 3, we can highlight the benefits of SOAP and SSB optimizers over the commonly used Adam and L-BFGS optimizers; by comparing Strategies 2, 3 and 4, we can quantify the importance of adaptive sampling within the MLT pipeline. Furthermore, Table 3 provides a comparative analysis of errors obtained using these various methods. Upon examining these results, it is evident that our method yields superior outcomes compared to the other methods.

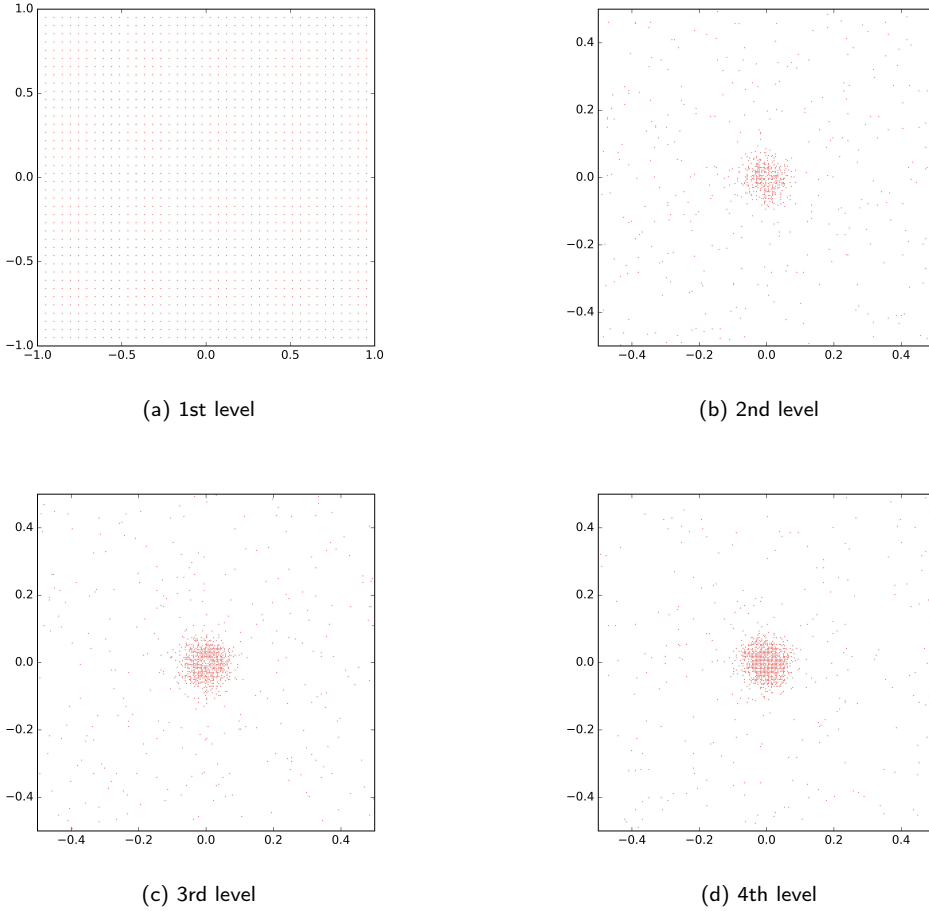


Figure 7: The sampling points at different levels for the two-dimensional Poisson equation with the solution Eq (46). This figure shows the behavior of 40×40 points in $[-0.5, 0.5]^2$.

4.4. Two-dimensional Helmholtz equation

For the following two-dimensional Helmholtz equation

$$\begin{cases} \Delta u(x, y) + k^2 u(x, y) = f(x, y), & (x, y) \text{ in } \Omega, \\ u(x, y) = 0, & (x, y) \text{ on } \partial\Omega, \end{cases} \quad (47)$$

where $\Omega = (-1, 1)^2$ and $k = 3$, the exact solution is given by

$$u = 4e^{-100(x^2+y^2)} \sin(6\pi x) \sin(6\pi y). \quad (48)$$

And the source function $f(x, y)$ is given by Eq (48).

In this experiment, we sample 10000 points within Ω as the residual training set and 1000 points on $\partial\Omega$ as the boundary training set, while utilizing 400×400 points for the test set and we employ a three-level framework for training. In the first-level pre-training, we trained 20000 epochs using the SOAP method. In the second-level training, we trained 20000 epochs of the SOAP method and 20000 epochs of the SSB method. Finally, in the third-level training, we employed 10000 epochs of the SSB method. During training at the different levels, we employed the MLS method described in Section 3.1.1 and the MLT method described in Section 3.1.2. Fig 10 illustrates the effect of the MLS method across the various levels; it can be seen that as the level increases, the points progressively concentrate toward

Multi-Level Deep Framework

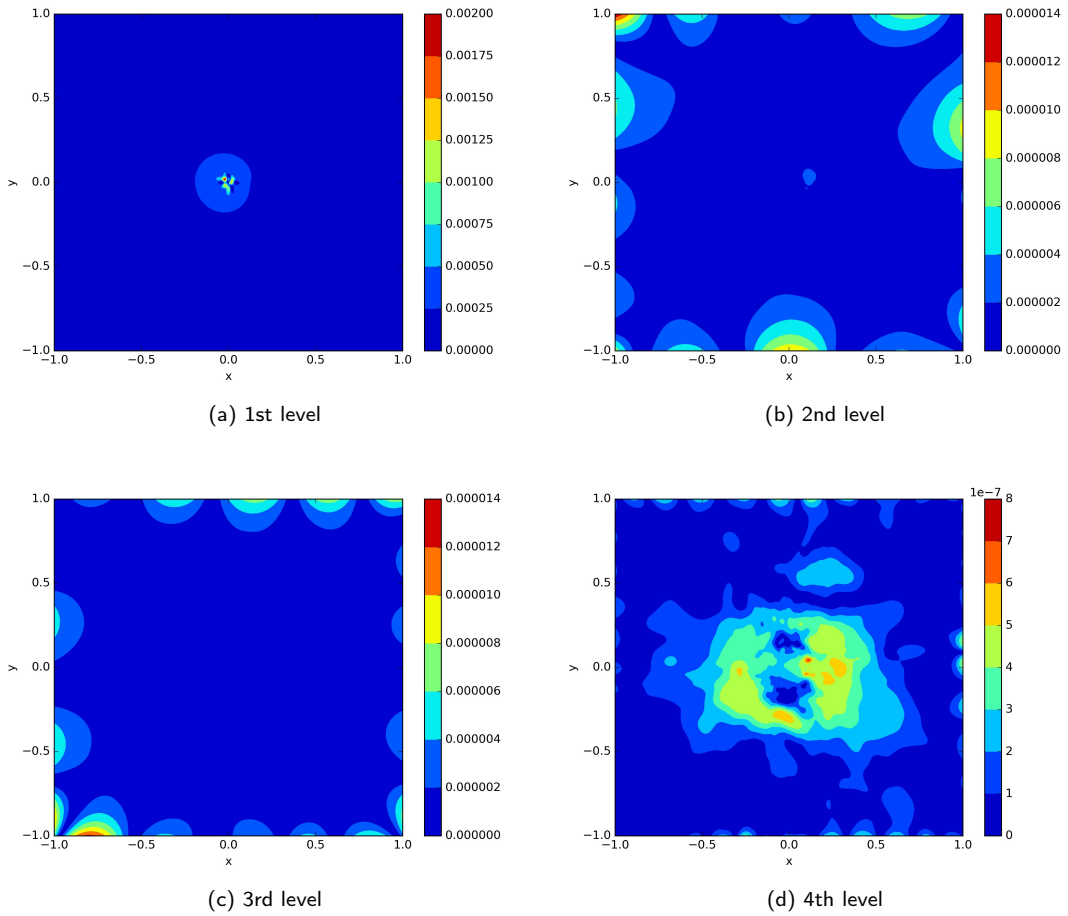


Figure 8: The numerical result of different levels for the two-dimensional Poisson equation with the solution Eq (46).

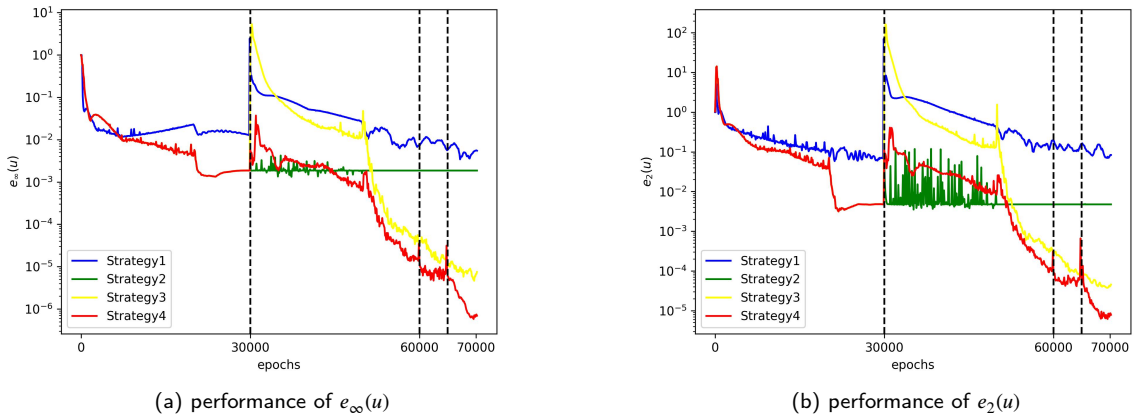


Figure 9: The performance of errors for the two-dimensional Poisson equation with the solution Eq (46). (a) the relative error $e_{\infty}(u)$ with different training epochs; (b) the relative error $e_2(u)$ with different training epochs.

Multi-Level Deep Framework

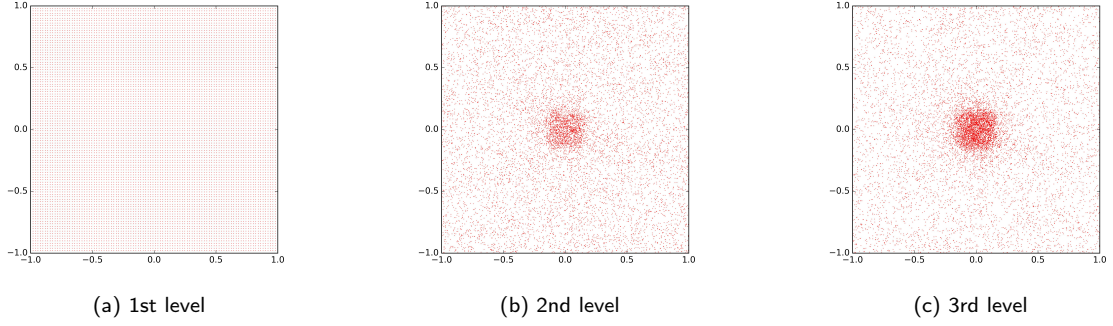


Figure 10: The sampling points at different levels for the two-dimensional Helmholtz equation with the solution Eq (48).

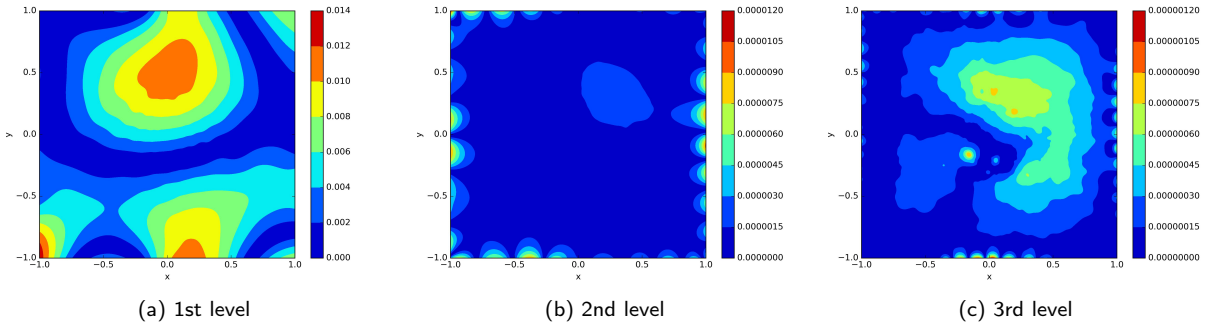


Figure 11: The numerical result of different levels for the two-dimensional Helmholtz equation with the solution Eq (48).

the origin, because the solution has very low regularity in the vicinity of the origin. It can be seen that the MLS method is able to capture this property effectively.

The numerical results of different levels are given in Fig 11. Fig 11 displays a heat-map based on absolute error $|\mathbf{u}^*(\mathbf{x}) - \mathbf{u}(\mathbf{x}; \theta)|$. It can be observed that as the level increases, the approximation error decreases, demonstrating the effectiveness of the MLT method.

To further highlight the advantages of our approach, we compare it here with three alternative strategies.

- Strategy 1 employs the MLS-PINN method: it pre-trains for 20000 Adam epochs, then performs two-level sampling, and finally trains again for 20000 Adam epochs and 30000 LBFGS epochs.
- Strategy 2 employs the MLS and MLT method with Adam and LBFGS optimizers: it pre-trains for 20000 Adam epochs, then performs two-level sampling, and trains again for 20000 epochs and 10000 LBFGS epochs, finally performs three-level sampling and trains again for 10000 LBFGS epochs.
- Strategy 3 optimizes with Soap and SSB optimizers while still following the MLS-PINN pipeline: it pre-trains for 20000 Soap epochs, carries out two-level sampling, and afterward trains for 20000 Soap epochs and 30000 SSB epochs.
- Strategy 4 is the multilevel framework that combines the MLS and MLT methods: it pre-trains for 20000 Soap epochs, uses MLS method to generate second-level sampling points and trains at that level for 20000 Soap epochs and 20000 SSB epochs, then uses MLS method to obtain third-level points and trains for 10000 SSB epochs.

Fig 12 shows the performance of these four strategies across training epochs. By comparing Strategy 1 with Strategy 3 and Strategy 2 with Strategy 4, we can demonstrate the advantages of SOAP and SSB over the commonly used Adam and L-BFGS optimizers. By comparing Strategy 1 with Strategy 2 and Strategy 3 with Strategy 4, we can quantify the

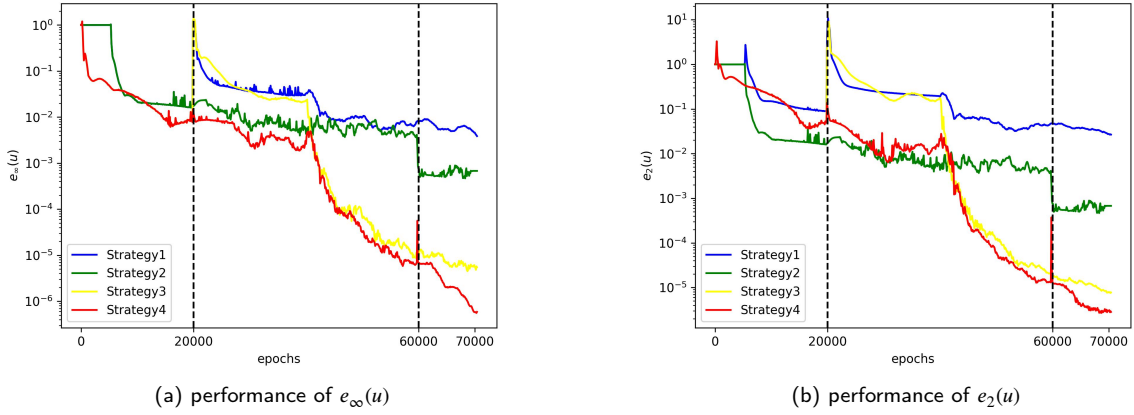


Figure 12: The performance of errors for the two-dimensional Poisson equation with the solution Eq (48). (a) the relative error $e_{\infty}(u)$ with different training epochs; (b) the relative error $e_2(u)$ with different training epochs.

Table 4

Comparison of errors using different methods for two-dimensional Helmholtz equation of Eq (48).

Relative error	Strategy 1	Strategy 2	Strategy 3	Strategy 4
$e_{\infty}(u)$	4.745×10^{-3}	5.031×10^{-4}	5.811×10^{-6}	6.916×10^{-7}
$e_2(u)$	2.758×10^{-2}	3.116×10^{-3}	7.875×10^{-6}	2.732×10^{-6}

benefits of the MLT training approach. Furthermore, Table 4 provides a comparative analysis of errors obtained using these various methods. Upon examining these results, it is evident that our method yields superior outcomes compared to the other methods.

4.5. Poisson Equation with Sharp Solutions

For the following Poisson equation [4],

$$\begin{cases} -\Delta u(x, y) = f(x, y), & (x, y) \text{ in } \Omega, \\ u(x, y) = g(x, y), & (x, y) \text{ on } \partial\Omega, \end{cases} \quad (49)$$

where $\Omega = (0, 1)^d$, the exact solution which has a peak at $(0, 0)$ is chosen as

$$u = 4^d \left(\frac{1}{2} + \frac{1}{\pi} \arctan \left(A \left(\frac{1}{16} - \sum_{i=1}^d \left(x_i - \frac{1}{2} \right)^2 \right) \right) \right) \prod_{i=1}^d (1 - x_i) x_i. \quad (50)$$

with $A=120$. The Dirichlet boundary condition $g(x, y)$ and the source function $f(x, y)$ are given by Eq (50).

4.5.1. Two-dimensional Problem

We take $d = 2$ in Eq (49) and (50) here. In this experiment, the network structure was adopted with a size of 32×8 . We sample 10000 points within Ω as the residual training set and 1000 points on $\partial\Omega$ as the boundary training set, while utilizing 400×400 points for the test set, and we employ a three-level framework for training. In the first-level pre-training, we trained 20000 epochs using the SOAP method. Then, in the second-level training, we again trained 20000 epochs of the SOAP method and 20000 epochs of the SSB method. Finally, in the third-level training, we employed 20000 epochs of the SSB method. During training at the different levels, we employed the MLS method described in Section 3.1.1 and the MLT method described in Section 3.1.2.

Fig 13 illustrates the effect of the MLS method across the various levels; it can be seen that as the level increases, the points progressively concentrate toward the origin, because the solution has very low regularity in the vicinity of the origin. It can be seen that the MLS method is able to capture this property effectively.

Multi-Level Deep Framework

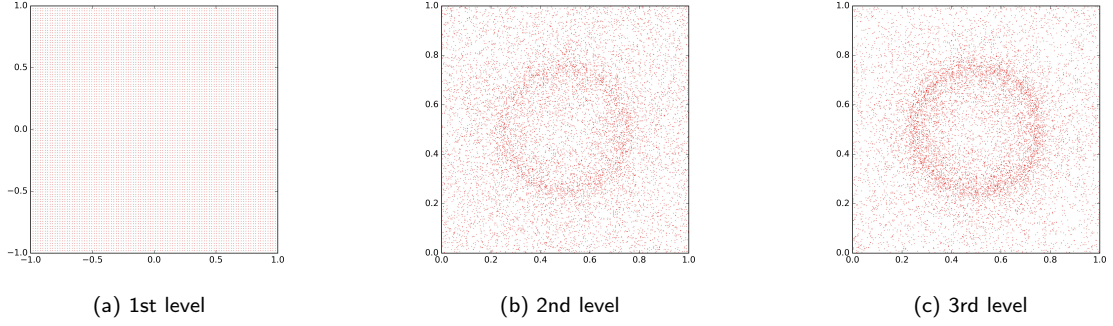


Figure 13: The sampling points at different levels for the two-dimensional Poisson equation with the solution Eq (50).

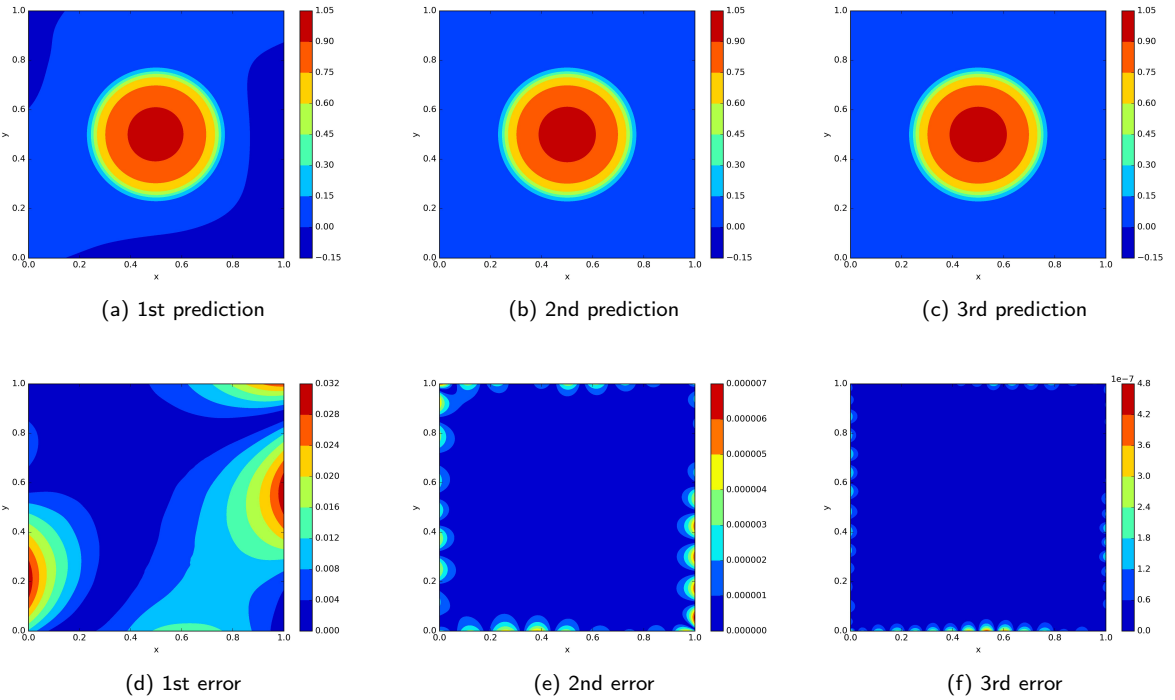


Figure 14: The numerical result of different levels for the two-dimensional Poisson equation with the solution Eq (50).

The numerical results of different levels are given in Fig 14. Fig 14 displays a heat-map based on absolute error $|\mathbf{u}^*(\mathbf{x}) - \mathbf{u}(\mathbf{x}; \theta)|$. It can be observed that as the level increases, the approximation error decreases, demonstrating the effectiveness of the MLT method. After three levels of training, the relative errors of the final predicted solution are $e_\infty(\mathbf{u}) = 4.400 \times 10^{-7}$ and $e_2(\mathbf{u}) = 8.197 \times 10^{-8}$. In [4], the best relative L^2 error result for problem 4.5 in the two-dimensional case is $e_2(\mathbf{u}) = 8.769 \times 10^{-7}$. In comparison, the accuracy of our method is superior.

4.5.2. Three-dimensional Problem

We take $d = 3$ in Eq (49) and (50) here. In this experiment, the network structure was adopted with a size of 32×8 . We sample 50000 points within Ω as the residual training set and 3000 points on $\partial\Omega$ as the boundary training set, while utilizing 160000 points for the test set, and we employ a three-level framework for training. In the first-level pre-training, we trained 20000 epochs using the SOAP method and 10000 epochs using the SSB method. Then, in

the second-level training, we again trained 20000 epochs of the SOAP method and 10000 epochs of the SSB method. Finally, in the third-level training, we employed 20000 epochs of the SSB method.

During training at the different levels, we employed the MLS method described in Section 3.1.1. Fig 15 illustrates the effect of the MLS method across the various levels; it can be seen that as the level increases, the points progressively concentrate toward the origin, because the solution has very low regularity in the vicinity of the origin. It can be seen that the MLS method is able to capture this property effectively.

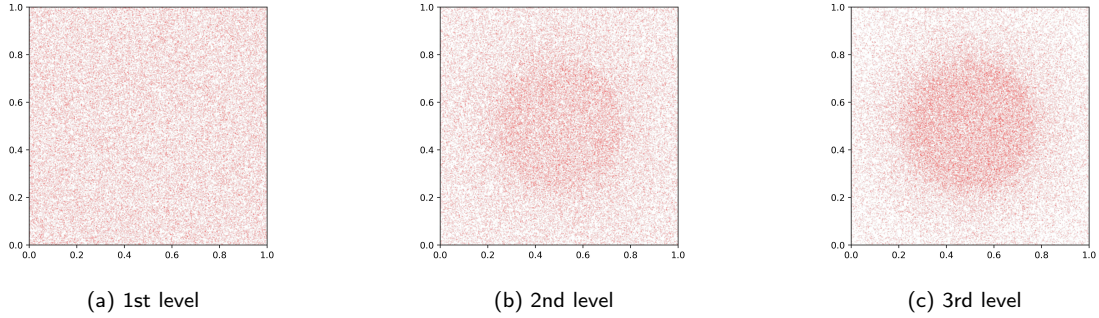


Figure 15: The sampling points at different levels for the three-dimensional Poisson equation with the solution Eq (50).

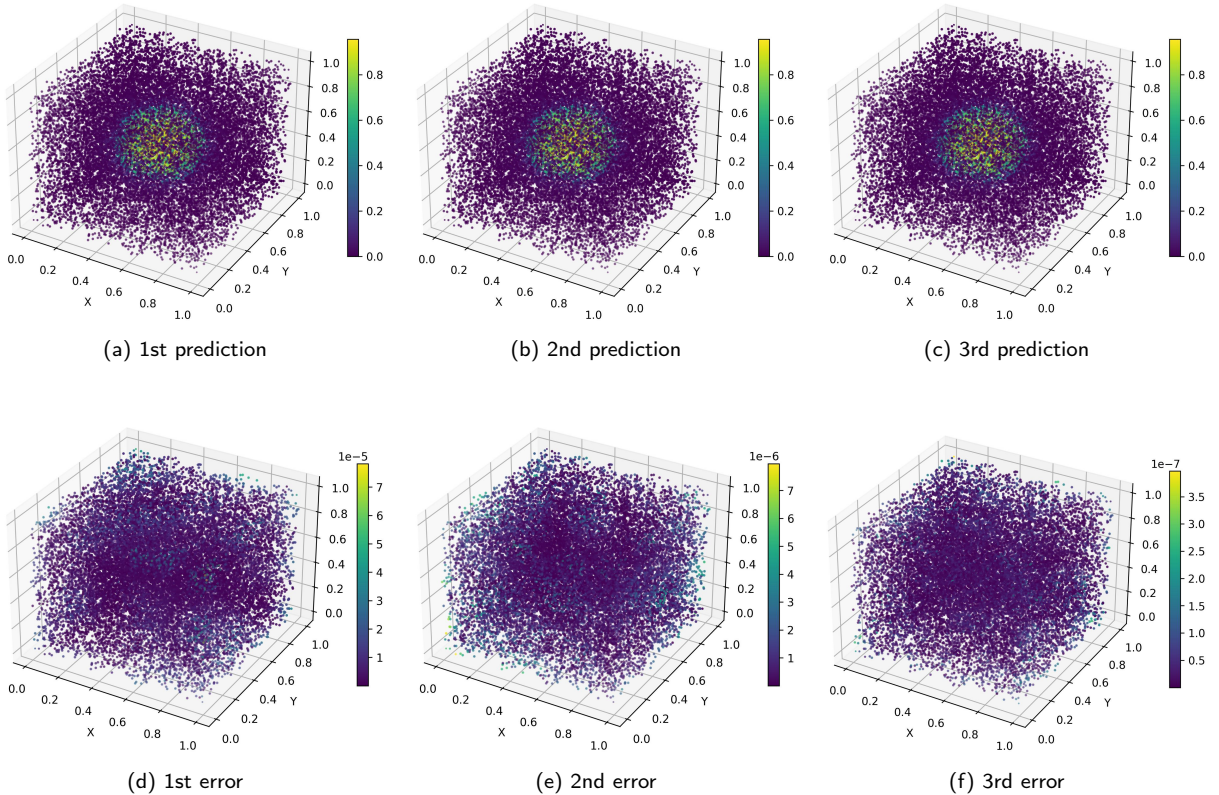


Figure 16: The numerical result of different levels for the three-dimensional Poisson equation with the solution Eq (50). For clearer visualization, only 20000 random points within the computational domain were sampled when generating this plot.

The numerical results of different levels are given in Fig 16. Fig 16 displays a heat-map based on absolute error $|\mathbf{u}^*(\mathbf{x}) - \mathbf{u}(\mathbf{x}; \theta)|$. It can be observed that as the level increases, the approximation error decreases, demonstrating the effectiveness of the MLT method. After three levels of training, the relative errors of the final predicted solution are $e_\infty(\mathbf{u}) = 8.707 \times 10^{-7}$ and $e_2(\mathbf{u}) = 1.442 \times 10^{-7}$. In [4], the best relative L^2 error result for problem 4.5 in the three-dimensional case is $e_2(\mathbf{u}) = 8.330 \times 10^{-4}$. In comparison, the accuracy of our method is superior.

4.6. Two-dimensional Poisson Equation with L shaped domain

For the following Poisson equation in two-dimension

$$\begin{cases} -\Delta u(x, y) = f(x, y), & (x, y) \text{ in } \Omega, \\ u(x, y) = g(x, y), & (x, y) \text{ on } \partial\Omega, \end{cases} \quad (51)$$

where the domain is L shaped $\Omega = (-1, 1)^2 \setminus (0, 1) \times (-1, 0)$, the exact solution is chosen as

$$u = r^{2/3} \sin \frac{2\theta}{3} - \frac{x^2 + y^2 - 2}{4}. \quad (52)$$

where r and θ are the coordinates in the polar coordinate system, i.e., $r = \sqrt{x^2 + y^2}$, $\tan(\theta) = \frac{y}{x}$.

In this experiment, we sample 7500 points within Ω as the residual training set and 1000 points on $\partial\Omega$ as the boundary training set, while utilizing 119600 points for the test set, and we employ a three-level framework for training. In the first-level pre-training, we trained 20000 epochs using the SOAP method. Then, in the second-level training, we again trained 10000 epochs of the SOAP method and 5000 epochs of the SSB method. Finally, in the third-level training, we employed 2500 epochs of the SOAP method and 12500 epochs of the SSB method.

During training at the different levels, we employed the MLS method described in Section 3.1.1. The large gradient of the solution near the origin is a major cause of difficulty in solving the problem. To mitigate the impact of the gradient term, we adjusted the parameters ($\gamma = 0.001, c = 0.1$) in the MLS method. Fig 17 illustrates the effect of the MLS method across the various levels; it can be seen that as the level increases, the points progressively concentrate toward $(0, 0)$, because the solution has very low regularity in the vicinity of $(0, 0)$. It can be seen that the MLS method is able to capture this property effectively.

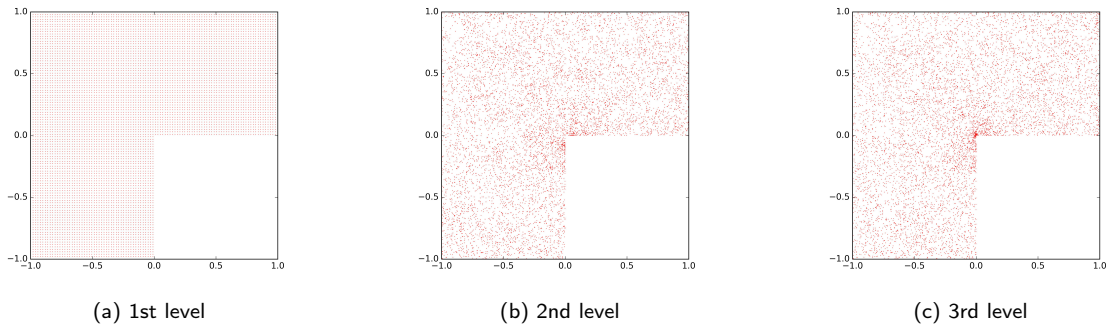


Figure 17: The sampling points at different levels for the two-dimensional Poisson equation with the solution Eq (52).

The numerical results of different levels are given in Fig 18. Fig 18 illustrates figures based on the predicted solutions $\mathbf{u}(\mathbf{x}; \theta)$ and the absolute error $|\mathbf{u}^*(\mathbf{x}) - \mathbf{u}(\mathbf{x}; \theta)|$. It can be observed that as the level increases, the approximation error decreases, demonstrating the effectiveness of our multi-level deep framework.

In Fig 19, we compare the commonly used RAD method in PINNs under the same number of training epochs. Specifically, the training process consists of pre-training with 20000 iterations of Adam optimizer, followed by sampling with the RAD method, finally trains again for 12500 Adam epochs and 17500 L-BFGS epochs. Fig 19 illustrates the variation of the relative errors during the training process, from which the superiority of our method can be observed. Ultimately, the relative errors of our method in solving the two-dimensional Poisson equation with the solution Eq (52) are $e_\infty(\mathbf{u}) = 2.209 \times 10^{-3}$ and $e_2(\mathbf{u}) = 2.716 \times 10^{-5}$.

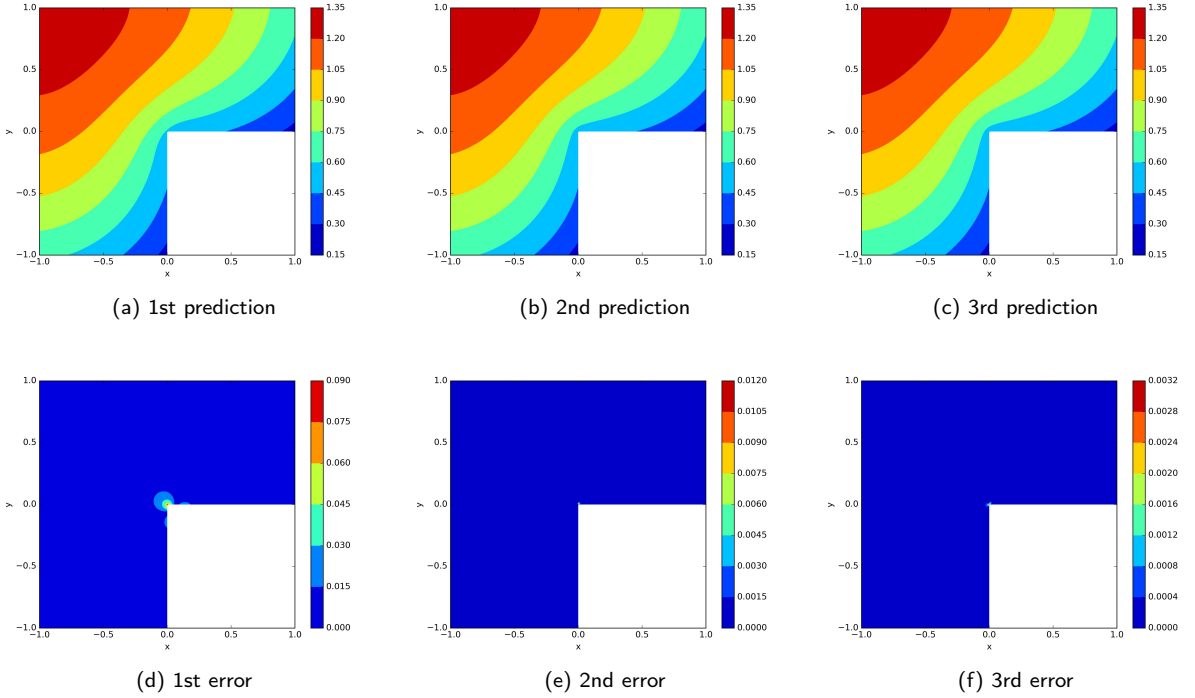


Figure 18: The numerical result of different levels for the two-dimensional Poisson equation with the solution Eq (52). (a)–(c) The predicted $u(x; \theta)$. (d)–(f) Performance of the absolute error $|u^*(x) - u(x; \theta)|$.

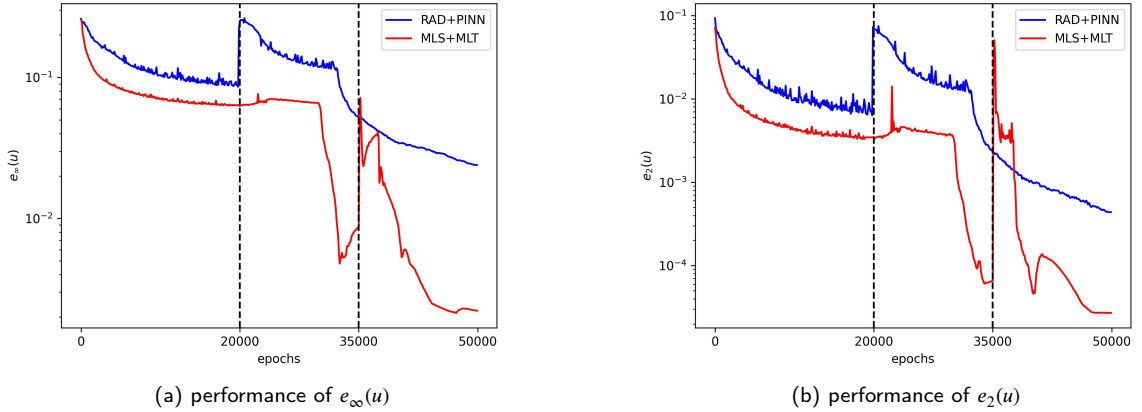


Figure 19: The performance of errors for the two-dimensional Poisson equation with the solution Eq (52). (a) the relative error $e_\infty(u)$ with different training epochs; (b) the relative error $e_2(u)$ with different training epochs.

4.7. Fourth-order Biharmonic equation

For the following Biharmonic equation in two-dimension

$$\begin{cases} -\Delta^2 u = f, & \text{in } \Omega, \\ u - \varepsilon_1 \partial_n(\Delta u) = 0, & \text{on } \partial\Omega, \\ \Delta u + \varepsilon_2 \partial_n(u) = 0, & \text{on } \partial\Omega, \end{cases} \quad (53)$$

where the domain is the unit disk $\Omega = \{(x, y) | x^2 + y^2 < 1\}$, and the source term is the Dirac function $\delta_{(0,0)}$. The exact solution is given by

$$u = \frac{r^2}{8\pi} \ln r + c_1 r^2 + c_2, \quad c_1 = \frac{1}{4 + 2\epsilon_2} \left(-\frac{1}{2\pi} - \frac{\epsilon_2}{8\pi} \right), \quad c_2 = -c_1 + \frac{\epsilon_1}{2\pi}. \quad (54)$$

where r and θ are the coordinates in the polar coordinate system.

In this experiment, we take $\epsilon_1 = \epsilon_2 = 10^{-5}$ and sample 100×100 points within Ω as the residual training set and 256 points on $\partial\Omega$ as the boundary training set, while utilizing 400×400 points for the test set, and we employ a three-level framework for training. In the first-level pre-training, we trained 20000 epochs using the SOAP method. Then, in the second-level training, we again trained 5000 epochs of the SOAP method and 10000 epochs of the SSB method. Finally, in the third-level training, we employed 300 epochs the SSB method.

During training at the different levels, we employed the MLS method described in Section 3.1.1. To enhance the concentration trend of the sampling points, we adjusted the parameters ($\gamma = 0, s = 1$) in the MLS method. Fig 20 illustrates the effect of the MLS method across the various levels; it can be seen that as the level increases, the points progressively concentrate toward $(0, 0)$, because the solution has very low regularity in the vicinity of $(0, 0)$. It can be seen that the MLS method is able to capture this property effectively.

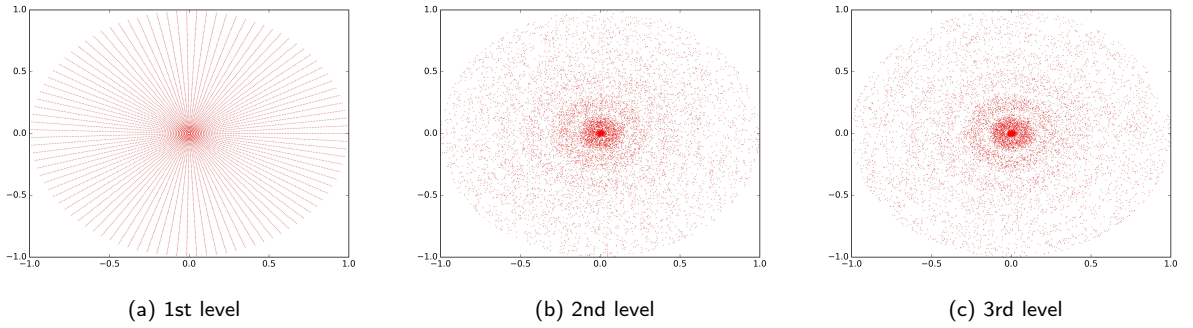


Figure 20: The sampling points at different levels for the two-dimensional Biharmonic equation with the solution Eq (54).

The numerical results of different levels are given in Fig 21. Fig 21 illustrates figures based on the predicted solutions $|\mathbf{u}(\mathbf{x}; \theta)|$ and the absolute error $|\mathbf{u}^*(\mathbf{x}) - \mathbf{u}(\mathbf{x}; \theta)|$. It can be observed that as the level increases, the approximation error decreases, demonstrating the effectiveness of our multi-level deep framework.

Ultimately, the relative errors of our method in solving the two-dimensional Biharmonic equation with the solution Eq (54) are $e_\infty(\mathbf{u}) = 1.651 \times 10^{-4}$ and $e_2(\mathbf{u}) = 4.774 \times 10^{-5}$.

4.8. Two-dimensional inviscid Prandtl equation

For the following unsteady Prandtl equations with zero pressure,

$$\begin{cases} u_t + uu_x + vv_y = 0, & 0 \leq x \leq 1, 0 \leq y \leq \infty, \\ u_x + v_y = 0 \\ v(x, 0, t) = 0 \\ u_0(x, y) = u(x, y, 0) = y + \sin 2\pi x. \end{cases} \quad (55)$$

In this inviscid problem, as [8], we specify a finite computational domain $\Omega = [0, 1] \times [0, 2] \times [0, 0.16]$ and impose periodic boundary conditions in x .

$$\begin{aligned} u(0, y, t) &= u(1, y, t), & 0 \leq y \leq 2, 0 \leq t \leq 0.16 \\ v(0, y, t) &= v(1, y, t) \end{aligned} \quad (56)$$

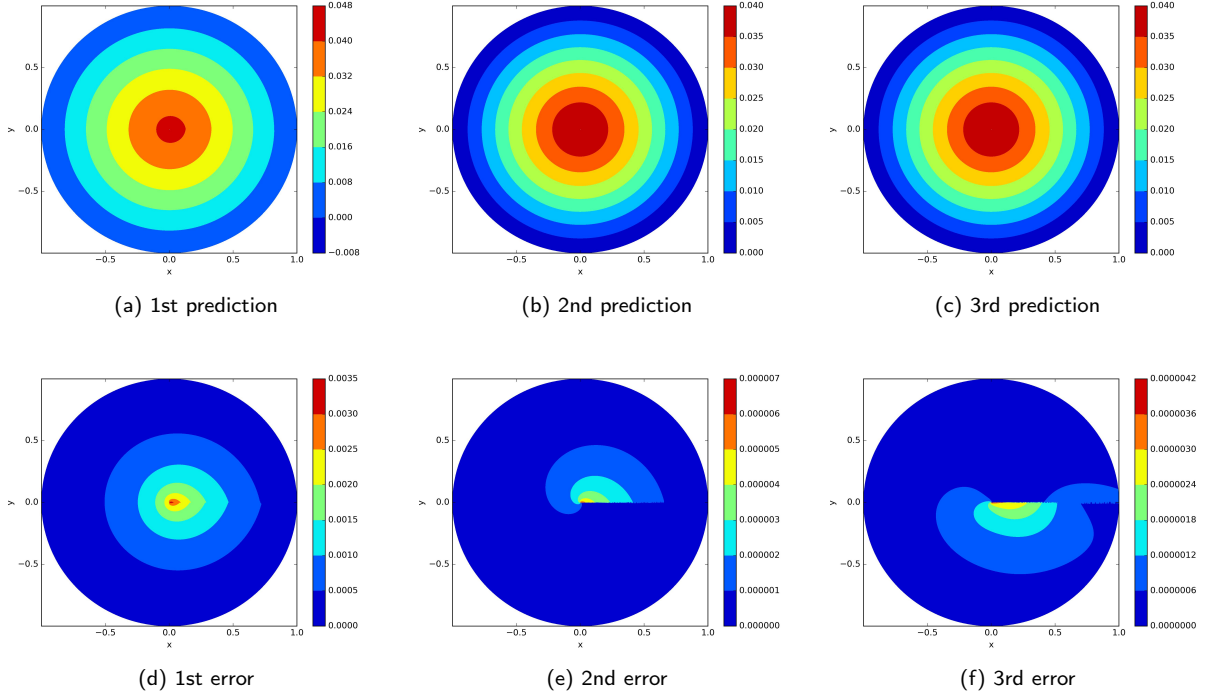


Figure 21: The numerical result of different levels for the two-dimensional Biharmonic equation with the solution Eq (54). (a)–(c) The predicted $\mathbf{u}(\mathbf{x}; \theta)$. (d)–(f) Performance of the absolute error $|\mathbf{u}^*(\mathbf{x}) - \mathbf{u}(\mathbf{x}; \theta)|$.

It is well known that, under general initial data, the inviscid Prandtl equation (55) does not admit a global smooth solution. In finite time, singularity arises from the compression of the fluid in the x -direction induced by nonlinear advection.

In this case, we will compare our numerical results with those reported in [8] (Fig 3.1). The governing equations and initial/boundary conditions used in our study are identical to those described in that reference. In Fig 3.1 of [8], the authors recast the inviscid Prandtl equations in conservation form 57a and explicitly discretize the resulting PDE in time.

$$u_t + (u^2)_x + (uv)_y = 0, \quad (57a)$$

$$u_x + v_y = 0 \quad (57b)$$

They evaluate the numerical x -flux for u^2 and adopt a Lax–Wendroff flux for the y -flux uv ; v is computed from u by integrating 57b, discretized using central differences. Further details of the scheme can be found in [8].

The challenge in the numerical solution lies in capturing the spike of $v(x, y, t)$ with breaking time $t = \frac{1}{2\pi} \approx 0.16$. Therefore, in this example we apply the multi-level learning framework only to v , while u is handled by the default approach—its values are recomputed at every level of training.

We sample 100000 points in Ω as the residual training set. And 100 points in each hyperplane on $\partial\Omega$. Additionally, we uniformly sample 20000 points on the boundary to softly enforce the periodic boundary condition in x , and another 10000 points to softly enforce the initial condition. At the same time, the boundary condition for $v(x, y, t)$ at $y = 0$ is imposed exactly (hard enforcement). In this experiment, during the first-level pre-training, we trained 20000 epochs using the SOAP method. In the second-level training, we trained 20000 epochs of the SOAP method and 30000 epochs of the SSB method. Finally, in the third-level training, we employed 50000 epochs of the SSB method. The distributions of residual sampling points are summarized in Fig 22.

In Fig 23, we present surface plots of the neural network predictions for $u(x, y, t)$ and $v(x, y, t)$ at $t = 0.16$ at different training levels. In Figure 24, we show two-dimensional graphs of the predictions of $u(x, y, t)$ and $v(x, y, t)$ at $y = 1$ for

Multi-Level Deep Framework

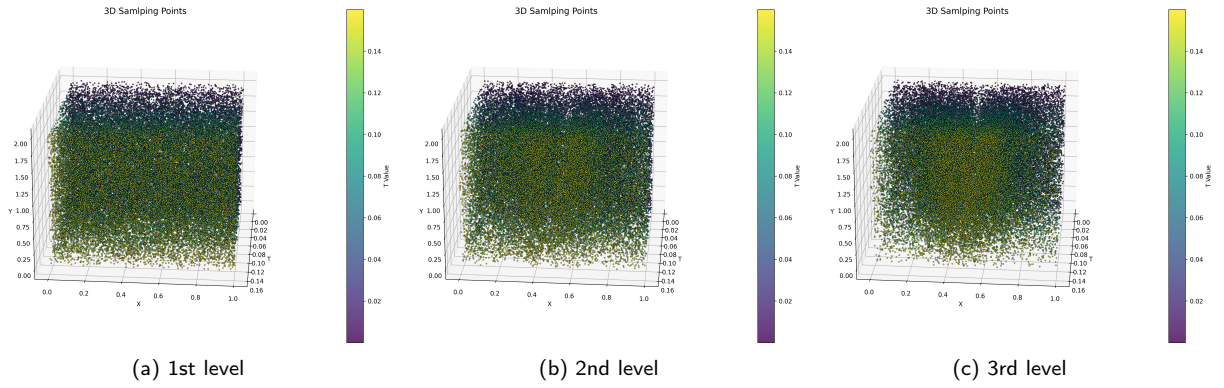


Figure 22: (a)-(c) The sampling points at different levels for two-dimensional inviscid Prandtl equation

$t = 0, 0.08, 0.16$, again at each level. By comparing Fig 3.1 in [8], it is immediately apparent that the results obtained with our method are comparable to the high-precision numerical scheme employed in [8]. A closer inspection of Fig 23 further reveals that our approach captures the spike of $v(x, y, t)$ even more accurately.

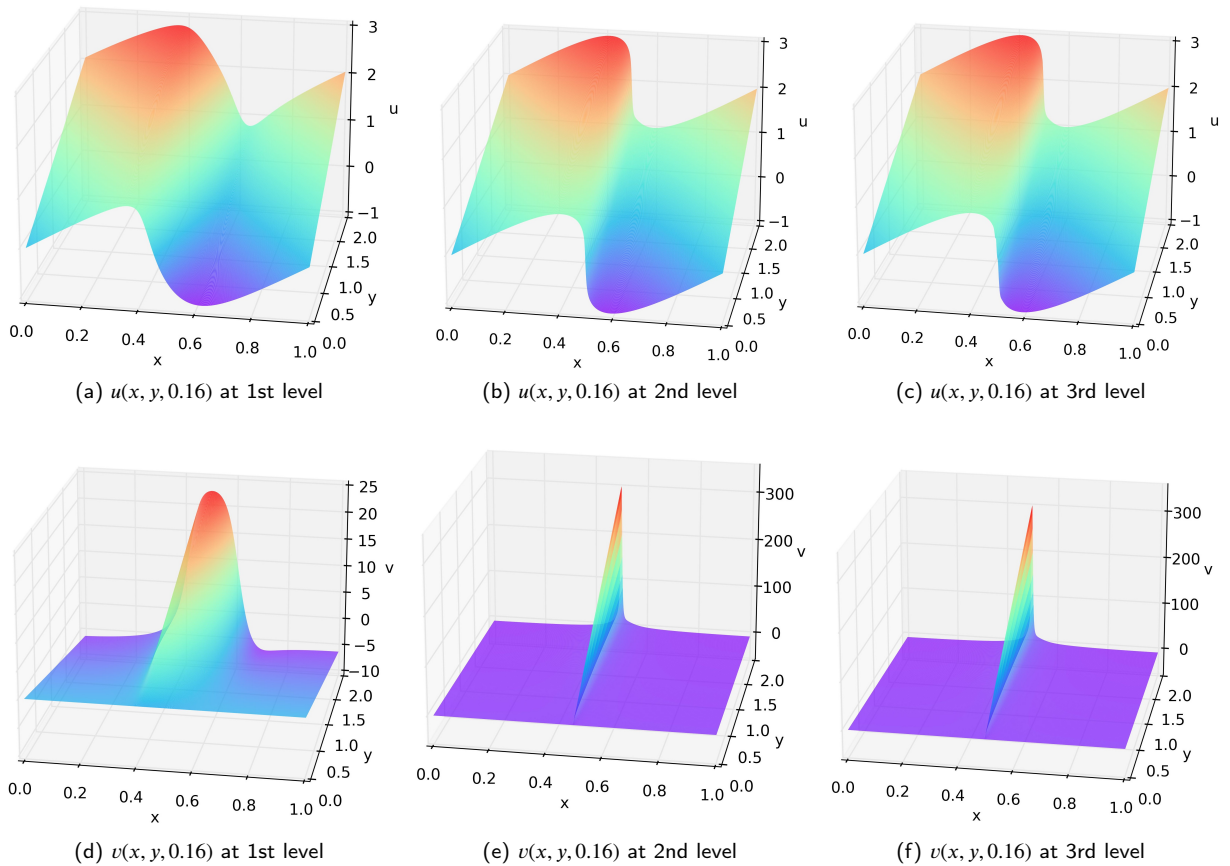


Figure 23: The surface plots of $u(x, y, 0.16)$ and $v(x, y, 0.16)$ at different levels for two-dimensional inviscid Prandtl equation.

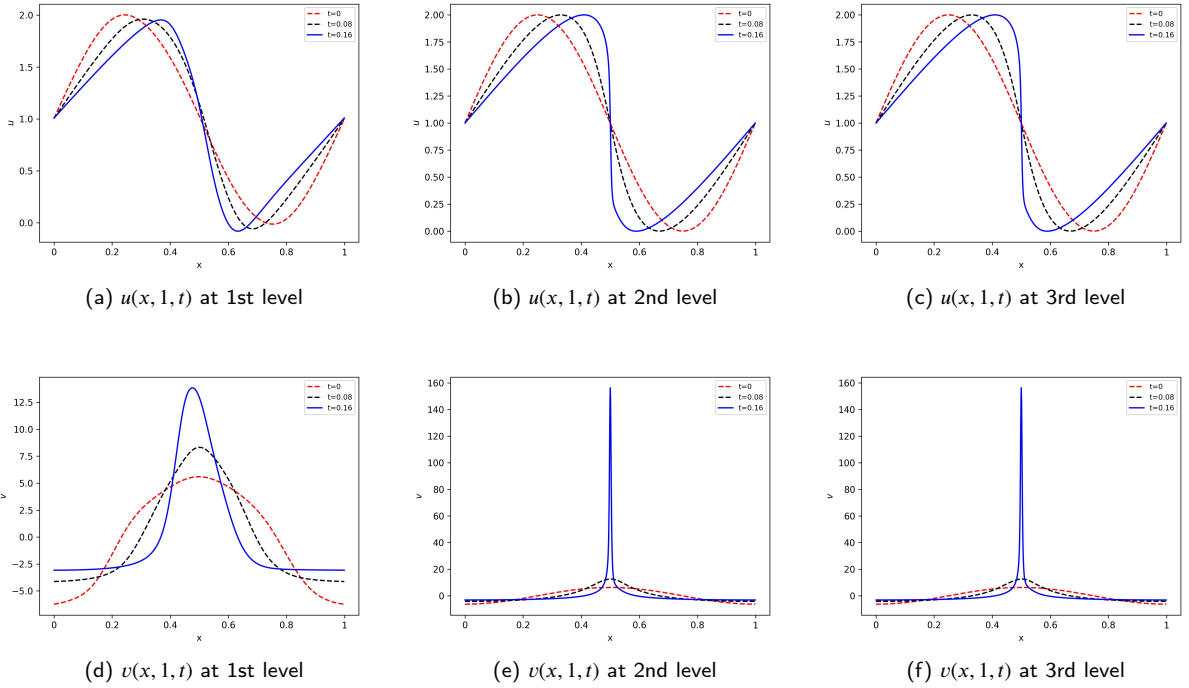


Figure 24: The plots of $u(x, 1, t)$ and $v(x, 1, t)$ at different levels for two-dimensional inviscid Prandtl equation.

4.9. Two-dimensional viscous Prandtl equation

For the following unsteady Prandtl equations with zero pressure,

$$\begin{cases} u_t + uu_x + vv_y = \nu u_{yy}, & 0 \leq x \leq 1, 0 \leq y \leq \infty, \\ u_x + v_y = 0, \\ u(x, 0, t) = v(x, 0, t) = 0, \\ u_y(x, y, t) \rightarrow 1, \quad \text{as } y \rightarrow \infty, \\ u_0(x, y) = u(x, y, 0) = y + \sin 2\pi x, \end{cases} \quad (58)$$

where $\nu = 0.1$.

In this viscous problem, as [8], we specify a finite computational domain $\Omega = [0, 1] \times [0, 2] \times [0, 0.16]$.

In this case, we will compare our numerical results with those reported in [8] (Fig 4.3). The governing equations and initial/boundary conditions used in our study are identical to those described in that reference. Further details of the scheme can be found in [8].

The challenge in the numerical solution lies in capturing the spike of $v(x, y, t)$ with breaking time $t = \frac{1}{2\pi} \approx 0.16$. Therefore, in this example we apply the multi-level learning framework only to v , while u is handled by the default approach—its values are recomputed at every level of training.

We sample 100000 points in Ω as the residual training set. Additionally, we uniformly sample 40000 points on the boundary to softly enforce the boundary condition in x , and another 5000 points to softly enforce the initial condition. At the same time, the boundary condition for $v(x, y, t)$ at $y = 0$ is imposed exactly (hard enforcement). In this experiment, during the first-level pre-training, we trained 20000 epochs using the SOAP method. In the second-level training, we trained 20000 epochs of the SOAP method and 30000 epochs of the SSB method. Finally, in the third-level training, we employed 50000 epochs of the SSB method. The distributions of residual sampling points as well as the behavior of the loss function across different training levels, are summarized in Fig 25.

Multi-Level Deep Framework

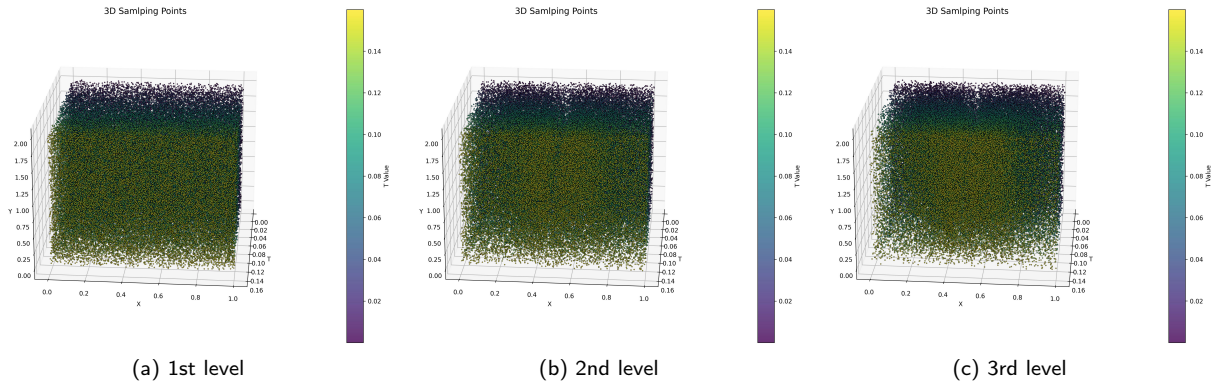


Figure 25: (a)-(c) the sampling points at different levels for two-dimensional viscous Prandtl equation.

In Fig 26, we present surface plots of the neural network predictions for $u(x, y, t)$ and $v(x, y, t)$ at $t = 0.16$ at different training levels. In Figure 27, we show two-dimensional graphs of the predictions of $u(x, y, t)$ and $v(x, y, t)$ at $x = 0.5$ for $t = 0.08, 0.16$ at each level. In Figure 28, we show two-dimensional graphs of the predictions of $u(x, y, t)$ and $v(x, y, t)$ at $y = 1$ for $t = 0, 0.08, 0.16$, again at each level.

By comparing Fig 4.3 in [8], it is immediately apparent that the results obtained with our method are comparable to the high-precision numerical scheme employed in [8]. A closer inspection of Fig 26 further reveals that our approach captures the spike of $v(x, y, t)$ even more accurately.

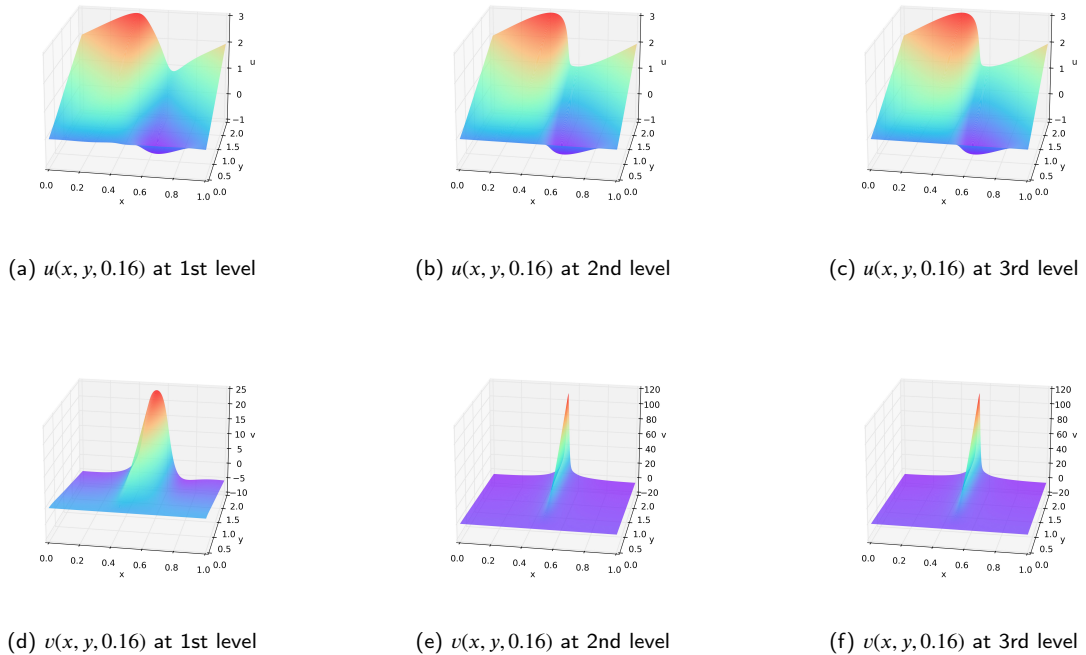
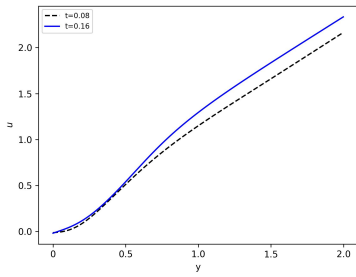
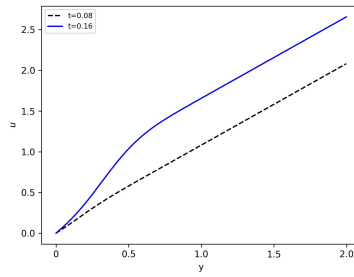


Figure 26: The surface plots of $u(x, y, 0.16)$ and $v(x, y, 0.16)$ at different levels for two-dimensional Prandtl equation.

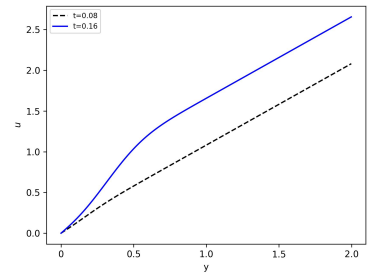
Multi-Level Deep Framework



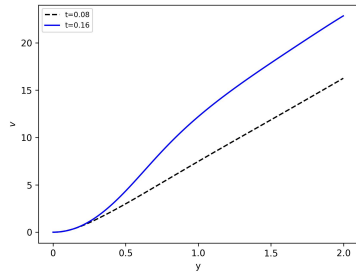
(a) $u(0.5, y, t)$ at 1st level



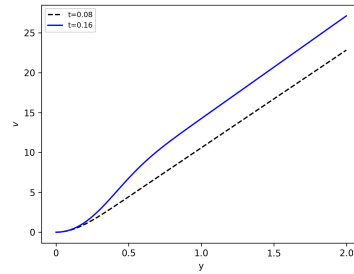
(b) $u(0.5, y, t)$ at 2nd level



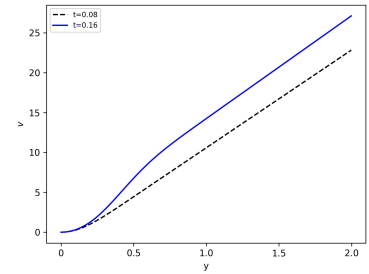
(c) $u(0.5, y, t)$ at 3rd level



(d) $v(0.5, y, t)$ at 1st level

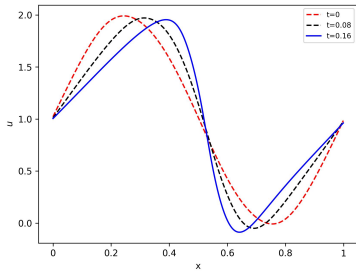


(e) $v(0.5, y, t)$ at 2nd level

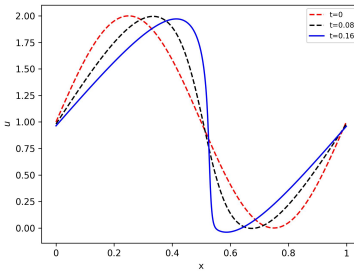


(f) $v(0.5, y, t)$ at 3rd level

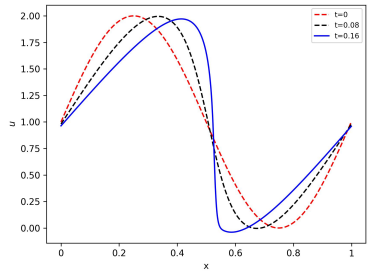
Figure 27: The plots of $u(0.5, Y, t)$ and $v(0.5, Y, t)$ at different levels for two-dimensional viscous Prandtl equation.



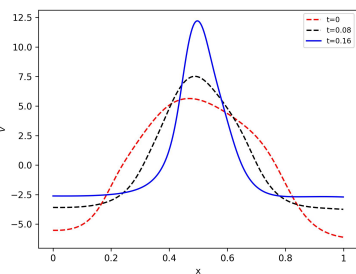
(a) $u(x, 1, t)$ at 1st level



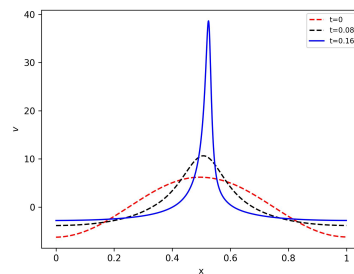
(b) $u(x, 1, t)$ at 2nd level



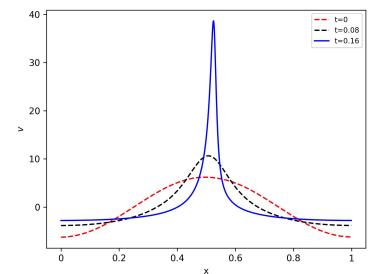
(c) $u(x, 1, t)$ at 3rd level



(d) $v(x, 1, t)$ at 1st level



(e) $v(x, 1, t)$ at 2nd level



(f) $v(x, 1, t)$ at 3rd level

Figure 28: The plots of $u(x, 1, t)$ and $v(x, 1, t)$ at different levels for two-dimensional viscous Prandtl equation.

5. Conclusions

In this paper, inspired by the multigrid method in traditional numerical methods, we have developed a framework that is distinct from the usual single training. This framework, known as the multilevel framework, consists of a multi-level sampling method based on residual and solution information, and a multi-level training method analogous to the multigrid method. Moreover, during the training process, we have introduced the advanced training methods, namely the SOAP method and the SSB method. Not only that, but we have also conducted a detailed theoretical analysis, theoretically proving the effectiveness of the proposed framework. Numerical experiments have demonstrated that our proposed method has significant advantages when dealing with low-regularity and high-frequency problems. In the future, we will focus on how to apply the multilevel framework to neural network models other than PINNs and on developing more intelligent multi-level sampling methods.

Acknowledgment

This research is partially sponsored by the National Key R & D Program of China (No.2022YFE03040002) and the National Natural Science Foundation of China (No.12371434).

Data Availability Statement

The data that support the findings of this study are available from the corresponding author upon reasonable request.

Conflict of Interest

The authors have no conflicts to disclose.

Appendix A

References

- [1] Al-Baali, M., 1998. Numerical experience with a class of self-scaling quasi-newton algorithms. *Journal of optimization theory and applications* 96, 533–553.
- [2] Al-Baali, M., Khalfan, H., 2005. Wide interval for efficient self-scaling quasi-newton algorithms. *Optimization Methods and Software* 20, 679–691.
- [3] Chen, Y., Dong, B., Xu, J., 2022. Meta-mgnet: Meta multigrid networks for solving parameterized partial differential equations. *Journal of computational physics* 455, 110996.
- [4] Dang, H., Wang, F., Jiang, S., 2024. Adaptive growing randomized neural networks for solving partial differential equations. *arXiv preprint arXiv:2408.17225*.
- [5] Dong, D., Suo, W., Kou, J., Zhang, W., 2024. Pinn-mg: A multigrid-inspired hybrid framework combining iterative method and physics-informed neural networks. *arXiv preprint arXiv:2410.05744*.
- [6] Gao, Z., Yan, L., Zhou, T., 2023. Failure-informed adaptive sampling for pinns. *SIAM Journal on Scientific Computing* 45, A1971–A1994.
- [7] He, J., Xu, J., 2019. Mgnet: A unified framework of multigrid and convolutional neural network. *Science china mathematics* 62, 1331–1354.
- [8] Hong, L., Hunter, J.K., 2003. Singularity formation and instability in the unsteady inviscid and viscous prandtl equations. *Commun. Math. Sci.* 1, 293–316.
- [9] Kingma, D.P., Ba, J., 2014. Adam: A method for stochastic optimization. *arXiv preprint arXiv:1412.6980*.
- [10] Li, Z., Kovachki, N.B., Azizzadenesheli, K., Bhattacharya, K., Stuart, A., Anandkumar, A., et al., . Fourier neural operator for parametric partial differential equations, in: *International Conference on Learning Representations*.
- [11] Liu, D.C., Nocedal, J., 1989. On the limited memory bfgs method for large scale optimization. *Mathematical programming* 45, 503–528.
- [12] Lu, L., Jin, P., Pang, G., Zhang, Z., Karniadakis, G.E., 2021. Learning nonlinear operators via deepnet based on the universal approximation theorem of operators. *Nature machine intelligence* 3, 218–229.
- [13] Raissi, M., Perdikaris, P., Karniadakis, G.E., 2019. Physics-informed neural networks: A deep learning framework for solving forward and inverse problems involving nonlinear partial differential equations. *Journal of Computational physics* 378, 686–707.
- [14] Sirignano, J., Spiliopoulos, K., 2018. Dgm: A deep learning algorithm for solving partial differential equations. *Journal of computational physics* 375, 1339–1364.
- [15] Tancik, M., Srinivasan, P., Mildenhall, B., Fridovich-Keil, S., Raghavan, N., Singhal, U., Ramamoorthi, R., Barron, J., Ng, R., 2020. Fourier features let networks learn high frequency functions in low dimensional domains. *Advances in neural information processing systems* 33, 7537–7547.
- [16] Tang, K., Wan, X., Liao, Q., 2020. Deep density estimation via invertible block-triangular mapping. *Theoretical and Applied Mechanics Letters* 10, 143–148.

- [17] Tang, K., Wan, X., Yang, C., 2023. Das-pinns: A deep adaptive sampling method for solving high-dimensional partial differential equations. *Journal of Computational Physics* 476, 111868.
- [18] Urbán, J.F., Stefanou, P., Pons, J.A., 2025. Unveiling the optimization process of physics informed neural networks: How accurate and competitive can pinns be? *Journal of Computational Physics* 523, 113656.
- [19] Vyas, N., Morwani, D., Zhao, R., Kwun, M., Shapira, I., Brandfonbrener, D., Janson, L., Kakade, S., 2024. Soap: Improving and stabilizing shampoo using adam. *arXiv preprint arXiv:2409.11321* .
- [20] Wainwright, M.J., 2019. *High-dimensional statistics: A non-asymptotic viewpoint*. volume 48. Cambridge university press.
- [21] Wang, Y., Lai, C.Y., 2024. Multi-stage neural networks: Function approximator of machine precision. *Journal of Computational Physics* 504, 112865.
- [22] Weinan, E., Yu, B., 2018. The deep ritz method: A deep learning-based numerical algorithm for solving variational problems. *Communications in Mathematics and Statistics* 6, 1–12.
- [23] Wu, C., Zhu, M., Tan, Q., Kartha, Y., Lu, L., 2023. A comprehensive study of non-adaptive and residual-based adaptive sampling for physics-informed neural networks. *Computer Methods in Applied Mechanics and Engineering* 403, 115671.
- [24] Xu, Y., 2025. Multi-grade deep learning. *Communications on Applied Mathematics and Computation* , 1–52.
- [25] Xu, Z.Q.J., 2018. Frequency principle in deep learning with general loss functions and its potential application. *arXiv preprint arXiv:1811.10146* .
- [26] Xu, Z.Q.J., Zhang, Y., Luo, T., 2024. Overview frequency principle/spectral bias in deep learning. *Communications on Applied Mathematics and Computation* , 1–38.
- [27] Yang, Y., Yang, Q., Deng, Y., He, Q., 2024. Moving sampling physics-informed neural networks induced by moving mesh pde. *Neural Networks* , 106706.
- [28] Zang, Y., Bao, G., Ye, X., Zhou, H., 2020. Weak adversarial networks for high-dimensional partial differential equations. *Journal of Computational Physics* 411, 109409.